DESIGN AND ANALYSIS OF NEW PRINTED WIDEBAND ANTENNAS FOR WIRELESS APPLICATIONS

A Dissertation
Submitted to the Graduate Faculty
of the
North Dakota State University
of Agriculture and Applied Science

By

Koby Asirvatham

In Partial Fulfillment
for the Degree of
DOCTOR OF PHILOSOPHY

Major Department:
Electrical and Computer Engineering

March 2014

Fargo, North Dakota

North Dakota State University
Graduate School

Title

DESIGN AND ANALYSIS OF NEW PRINTED WIDEBAND ANTENNAS FOR WIRELESS APPLICATIONS

By

Koby Asirvatham

The Supervisory Committee certifies that this ***disquisition*** complies with North Dakota State University's regulations and meets the accepted standards for the degree of

DOCTOR OF PHILOSOPHY

SUPERVISORY COMMITTEE:

Dr. Benjamin D. Braaten
Chair

Dr. David A. Rogers

Dr. Jacob Glower

Dr. Michael Reich Dr. Nikita Barabanov

Approved:

3/12/2014
Date

Dr. Scott Smith
Department Chair

ABSTRACT

In this study a simple method to develop a wideband antenna is proposed. With this new technique a dipole antenna with a 48% frequency bandwidth is transformed to achieve a 120% frequency bandwidth for a voltage standing-wave ratio ≤ 2. Two different designs are tested and their performance is compared: the segmented-ring antenna and the split-ring antenna. Both antennas achieved a stable radiation pattern and a moderate gain. Nearly omnidirectional radiation patterns have been observed in both the XZ and YZ-planes. Finally, simple passive arrays are presented, demonstrating the usefulness of the split-ring antenna as an array element. Beam steering is demonstrated with a four element passive array using horizontal meandering lines. This novel antenna has wide applications in high-capacity wireless communication system.

ACKNOWLEDGMENTS

First and foremost I wish to thank my advisor, Dr. Braaten for accepting me into the program, helping me to come up with the thesis topic, guiding me and for giving me the moral support and the freedom I needed to move on.

I am indebted to Dr. Rogers, Dr. Glower, Dr, Reich and Dr. Barabanov for serving on my graduate committee. Regardless of their growing responsibilities in their own work, they were always willing to take time for adding new ideas to my project.

A very special thanks to Dr. Rogers for giving close attention and guidance to technical quality**,** quality of written English and overall structure of the thesis.

A special gratitude to Dr. Reich and engineer Nate Schneck at CNSE, for their care and expertise in fabricating the antennas. Without good milling, good measurements would not have been possible. A special thanks again to Dr. Reich for the far-field radiation pattern measurements, teaching me experimental techniques, and thoughtful comments and suggestions. I am also indebted to Dr. Maassel for arranging time with CNSE, providing transport, companionship, advice and assisting in antenna measurements.

I am very thankful to Dr. Glower and the chair, Dr. Smith for giving me an opportunity to teach classes at NDSU with full classroom responsibility. This is the most gratifying experience I have ever had, as a PhD student at NDSU, and it was worth going to school here just for that.

Many thanks to my close friends, classmates, professors and staff members who have made learning more fun than ever. Last but not least, I am forever indebted to my family in Malaysia who have encouraged and inspired me all along in my academic endeavors.

DEDICATION

To the SELF in all selves

TABLE OF CONTENTS

ABSTRACT iii

ACKNOWLEDGMENTS iv

DEDICATION v

LIST OF FIGURES viii

LIST OF APPENDIX FIGURES xi

CHAPTER 1. INTRODUCTION 1

Wideband Antennas 1

Ultra-wideband Radio Technology 2

Bandwidth Enhancement 4

CHAPTER 2. THE DEVELOPMENT OF SEGMENTED RING ANTENNA 8

Planar Spiral Antenna 8

Segmented-ring Antenna 10

Circuit Model of Segmented-ring Antenna 19

Design and Analysis of the Segmented-ring Antenna 24

Conclusion – The Segmented-ring Antenna 28

CHAPTER 3. SPLIT-RING ANTENNA 30

Split-Ring Antenna Design 31

Circuit Model of Split-ring Antenna 38

Split-ring Layout Design.....38

Design and Analysis of the Split-ring Antenna 39

CHAPTER 4. DIPOLE ANTENNA ARRAY.....41

Dipole Antenna Array Design 41

CHAPTER 5. SPLIT-RING ANTENNA ARRAY 45

CHAPTER 6. FABRICATION AND MEASURMENT.....52

CHAPTER 7. DISCUSSION AND CONCLUSION 56

BIBLIOGRAPHY.....58

APPENDIX A. DERIVATION OF FAR-FIELD ELECTRIC FIELD 63

Short Dipole.....63

Dipole of Arbitrary Length.....64

APPENDIX B. DERIVATION OF SEGMENTED-RING ANTENNA CIRCUIT MODEL SHOWN IN FIG. 19……..69

LIST OF FIGURES

Figure Page

1. A portable device with three separate antennas. ……2
2. Frequency allocation of UWB and other existing wireless systems...……...…..…….3
3. International spectrum allocation for UWB bands 2009…….4
4. Schematic of the quasi-Yagi antenna……..7
5. ADS 3D model planar spiral antenna……..9
6. ADS model planar spiral antenna.……..…….9
7. Simulated reflection coefficients of dipole and spiral antenna……..10
8. Feeding system without antenna.....…….…….…….11
9. The evolution of the segmented ring antenna (exact relative sizes)……..12
10. Simulated reflection coefficients of spiral antennas and segmented-ring antenna...…….12
11. ADS model of wideband segmented-ring antenna ……..…….14
12. Schematic of wideband segmented-ring antenna……...15
13. Photograph of an S-band and C-band segmented-ring……...…16
14. Lumped-element model, layout and measured S-parameters……....16
15. Measured and simulated radiation patterns of segmented ring antenna and dipole antenna's simulated far-field patterns (c, f, I, and l) at 2.5, 4.5, 6.5 and 7.5GHz…….18
16. Simulation of antenna's relative gain along the z-axis..……....19
17. Dipole antenna model resonating at 2.7 GHz……20
18. Segmented ring antenna lumped-element circuit model……21
19. Simplified segmented ring antenna lumped-element circuit model……..21

20. Lumped-element circuit model reflection coefficients…….……....22

21. Segmented-ring lumped-element circuit model reflection coefficients for various series inductor ($L_1/2$) values……23

22. Segmented-ring lumped-element circuit model reflection coefficients for various shunt capacitor (C_{sh}) values……..……....23

23. Segmented-ring (a) Magnitude of input impedance (b) Real part of the input impedance (c) Imaginary part of the input impedance (d) Input reflection coefficient....24

24. Segmented-ring antenna's reflection coefficient at the feed gaps: h = 0.6 and h = 2.65mm ……..25

25. Segmented-ring antenna's reflection coefficient for different mean ring radii…….25

26. Segmented-ring antenna's parameter adjustment and the corresponding reflection coefficients……26

27. Split-ring antenna surface current pattern at 2.1, 4.5 and 7.5 Ghz……28

28. ADS model of wideband split-ring antenna……..32

29. Schematic of wideband split ring antenna…….33

30. Photograph of an S-band and C-band split-ring antenna…….……..33

31. Photograph split-ring antenna and segmented-ring antenna……..34

32. Simulation and measured input reflection coefficient of the prototype split-ring antenna……...34

33. Measured and simulated radiation patterns of split-ring antennas at 2.5, 4.5, 6.5 and 7.5 GHz…..……36

34. Measured radiation patterns of split-ring and segmented ring antennas at 2.5, 4.5, 6.5 and 7.5 GHz……..37

35. Simulation of antenna's relative gain along the z-axis……..38

36. Split-ring antenna surface current pattern at 2.1, 4.5 and 7.5 GHz……40

37. ADS model of dipole antenna, XZ-cut and input reflection coefficient……43

38. Fig. 38. Simulated input reflection coefficient and XZ-cuts of four element dipole antenna array: (a) Without beam steering (b) With meandering line beam steering (c) With meandering line beam steering plus additional beam steering from the phase shifter network……...44

39. Simulated XZ-cut of eight element dipole antenna array at 9 GHz……...44

40. ADS layout of four-element split-ring antenna array for broadside beam…….....46

41. ADS layout of four-element split-ring antenna array with delay lines for tilted beam….46

42. Photograph of four-element split-ring antenna array for broadside beam…….46

43. Photograph of four-element split-ring antenna array with delay lines for broadside beam……..47

44. Measured input reflection coefficient for broadside and tilted beam of split-ring antenna arrays……....47

45. Measured and simulated radiation patterns of split-ring antenna broadside-beam array at 2.5, 4.5 and 6.5 GHz…….……...…..48

46. Measured and simulated radiation patterns of split-ring antenna tilted-beam array at 2.5, 4.5 and 6.5 GHz……..……49

47. Broadside and tilted-beam radiation patterns at 2.5 and 4.5 GHz…….50

48. Simulated relative gain along the z-axis……51

49. Anechoic chamber used for antenna measurement……53

50. Segmented ring antenna mounting system……53

51. Close-up view of split ring antenna mounting system……...54

52. Close-up view split ring antenna array mounting system……..54

53. ADS model segmented ring antenna, XZ-cut and YZ-cut……..…...55

54. ADS split ring antenna array model……..55

LIST OF APPENDIX FIGURES

Figure Page

A1. Short dipole placed at the origin of a spherical coordinate system ..……..……...63

A2. Current distribution for three center-fed dipoles……..64

A3. Center-fed dipole of length *l*……65

CHAPTER 1. INTRODUCTION

The antenna is an essential part of any wireless system because it is the device that launches a propagating electromagnetic wave into free space. Studies have shown that microstrip printed patch antennas are of compact size, low profile, low fabrication cost, reduced weight, semi omnidirectional and simple feed ability, which enable them easy integration with microwave integrated circuits [1], but they are known to have a narrow impedance bandwidth. However, with current advancements in antenna design tool and fabrication technologies, various bandwidth widening techniques are available. The rapid development in wireless communication technologies call for the addition of more than one communication system into a single compact module. This signifies that the future communication antennas should meet the requirements of multi-band or wideband capability to cover the several operating bands [2] or to operate as a high capacity antenna.

Wideband Antennas

Present-day telephone, satellite, and internet technology companies are offering services that were not available only a few decades ago. Modern satellite, wireless communications, and radar systems often demand wideband performance for multi-channel and high data capacity operations. These main companies' main goal is to produce an all-in-one portable and compact device for users. This requires wireless systems to operate in several bands or in a continuous band such as the ultrawide-band system. For the multi-channel purposes, a portable wireless communication device will require several antennas resonating at several different narrow frequency bands. These antennas are often limited by size and bandwidth, and thus pose additional challenges to ever shrinking portable devices that demand wideband performance and

the capability of receiving and transmitting at multiple bands. Fig. 1 is an example of a portable device with three separate antennas performing the task of receiving and transmitting wireless signals for five different frequency bands [3]. As the commercial demand for multiple band increases, creating a single antenna for every separated narrow bands of interest is not economical. One solution is to create a multi-band compact system to combine a variety of different narrow band operational modes into a single antenna that is tuned to multiple narrow bands of interest.

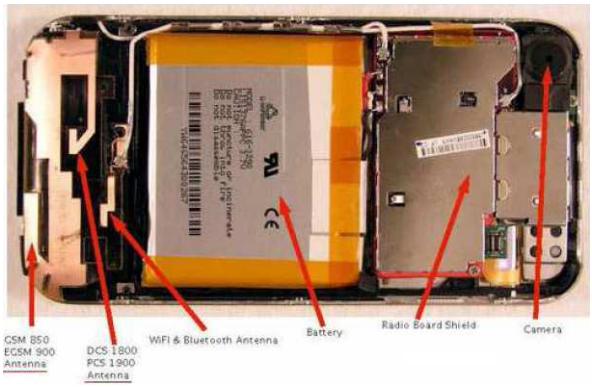

Fig. 1. A portable device with three separate antennas.

Ultra-wideband Radio Technology

Ultra-Wide Band (UWB) wireless communications technology is over thirty years old. It was restricted for usage in precise radar tracking and some other military applications [4] until 2002. The approval of a 7.5 GHz unlicensed spectrum by US Federal Communications Commission (FCC, 2002) for commercial and academic development has sparked vigorous research and development activity of UWB technology for short-range wireless communications, imaging, radar, remote sensing, and localization applications. The UWB antenna utilizes the entire spectrum for transmitting data. Hence, more data is transmitted in a given period of time than the narrow band antenna. The maximum allowable power spectral density (PSD) for UWB

transmission is -41.3 dBm/MHz. Nevertheless, the potential for exploiting such low power UWB links for high data rate wireless connectivity (in excess of 100 Mbps) at ranges up to 10 m, particularly for in-home networking applications, has led to considerable recent interest in this technology. For example, 0.56 mW of power spread across 7.5 GHz of spectrum puts only 0.075 pW of power into each hertz band of frequency. The power at any frequency is below the acceptable noise floor. Thus, UWB can coexist with other RF technologies, because it appears only as noise [5]. Frequency allocation of UWB and other existing wireless system is shown in Fig. 2 [6]. The UWB frequency mask and the allowed power level are about the same for Europe, UK, US, Germany, Japan, Korea and Singapore, but not all are unlicensed [7]. International Spectrum Allocation for UWB Bands 2009 in some countries is shown in Fig. 3 [8].

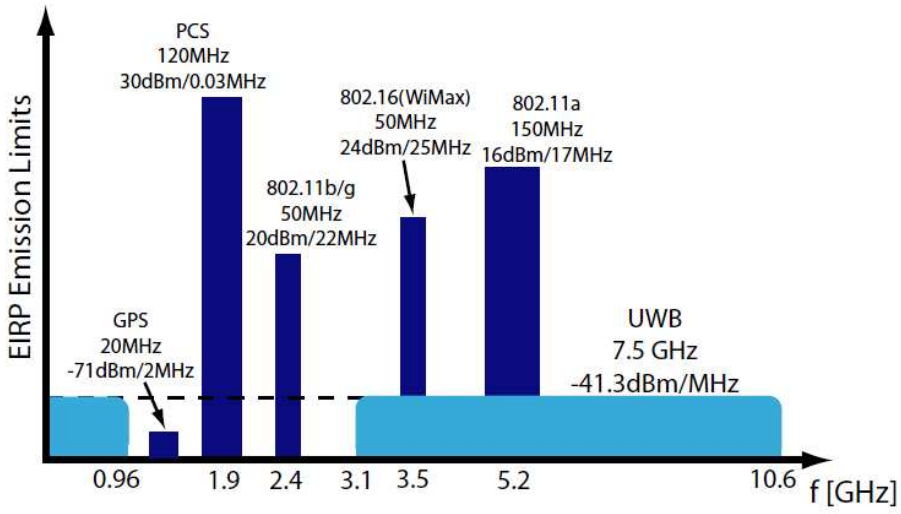

Fig. 2. Frequency allocation of UWB and other existing wireless systems in USA.

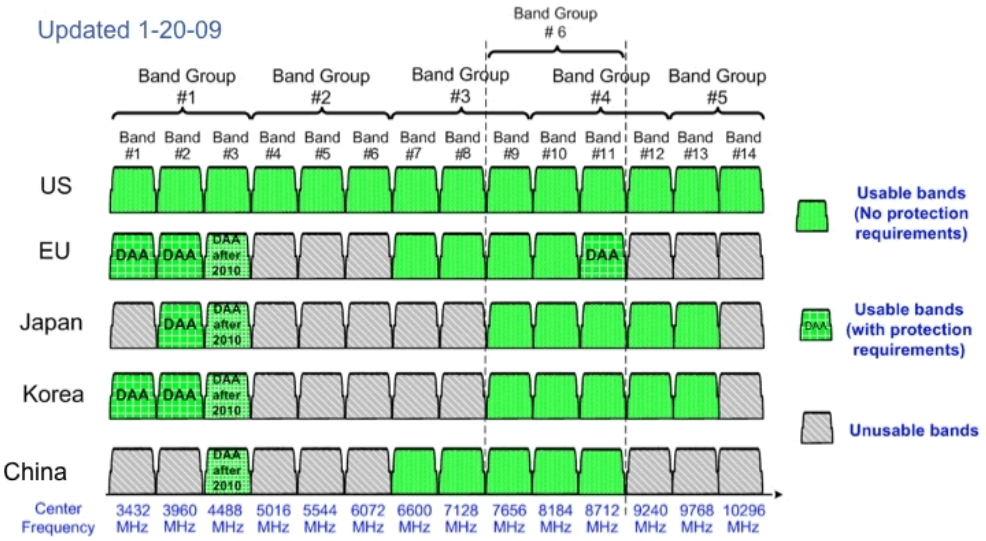

Fig. 3. International spectrum allocation for UWB bands 2009.

Bandwidth Enhancement

There is a particular interest to design antenna arrays with increased operational bandwidth in view of increasing demand for the wideband application. The conventional microstrip patch is not a good candidate for wideband mobile wireless applications due to its narrow bandwidth. Therefore, more unusual approaches are being investigated for multiband antenna with reduced size operation. Several bandwidth enhancement techniques have been studied to keep up with the trend. Prior to a brief survey of some of these techniques, it is worth defining a standard bandwidth. The impedance bandwidth is the range of frequencies over which the input impedance conforms to a near perfect match and hence maximum power transfer. The commonly accepted standard is a voltage standing-wave ratio with a VSWR ≤ 2 where the reflected power is about 10 %. The operating bandwidth of the antenna could be smaller than the impedance bandwidth, since other parameters such as gain, beam width, radiation patterns and polarization are also functions of frequency and may deteriorate over the impedance bandwidth. Impedance bandwidth is also termed the fractional bandwidth of an antenna. It is a measure of

how wideband the antenna is. In general, the fractional bandwidth and center frequency is defined as

$$FBW = \frac{f_u - f_l}{f_c} \times 100\%$$
$$f_c = \frac{f_u + f_l}{2}, \quad (1)$$

where f_u and f_l are the upper and lower frequencies, and f_c is the design frequency or center frequency [9].

Recently, a bandwidth enhancement technique using transmission line coupling to a slot line was proposed in [10]. This design achieved a fractional bandwidth of 45.6 % (1.54 – 2.45 GHz). This design involves a complex geometry occupying a substrate area of 89.5 mm by 20 mm. A printed log-periodic antenna, employing fourteen-dipole arrays measuring a total area of 114 mm by 30 mm was presented in [11]. The antenna's bandwidth was 100 % (4.25 -14.25 GHz). The main drawbacks are the use of a large areas to accommodate the radiators and feed line, and the difficulty involved in the design of the double-sided dipole arrays. The introduction of capacitive coupling between the spiral radiating element and the ground plane was reported in [12]. A bandwidth of 66% (6.27- 12.47 GHz) was observed with a substrate area of 40 mm by 50 mm. The work involved in the optimization of the design parameters of the antenna structure is quite elaborate. Notching the ground plane is a common method used for increasing the bandwidth of antennas [13,14]. Great care is required in the ground plane design, and to form coupling between the patch and the transmission line. The achieved bandwidth in [13] is 129 % (520 – 2400 MHz) with an antenna size of 106 mm by 65 mm. A very recent method to increase the bandwidth of the antenna in the S and C bands is presented in [15]. Complicated modeling is

used to design the defected ground structure to alter the current distribution. The achieved bandwidth is 44% (3.2 - 4.8 GHz), with a total area of approximately 60 mm by 43 mm. A new shorted patch antenna with shorting pins with a 3D structure (28 mm by 10mm by 7 mm) is introduced in [16]. The achieved bandwidth is 94.17% (4.13–11.48 GHz). This design has many mechanical parts that can make the design, optimization and assembly process very cumbersome. A frequency-reconfigurable 2–8 GHz band Archimedean spiral antenna is presented in [17]. The feeding structure of this antenna involves additional design considerations. In addition to that the antenna has a two-arm Archimedean spiral with four numbers of turn, thus complicating the design and fabrication process. The overall size of the spiral antenna is 60 mm by 69 mm. A wideband microstrip patch antenna for S and C application is reported in [18]. The antenna is a 3D structure measuring 17.2 mm by 16.4 mm by 7.6 mm, and is based on a the gap coupled cavity structure. It involves a sophisticated modeling and fabrication process. The antenna achieved a bandwidth of 50%. Based on these reviews, most of the bandwidth improvement techniques involve additional design considerations, structural complexity, a large area, and the bandwidth achieved is not very impressive for the amount of design work or the fabrication complexity involved. To overcome these short comings we have recently proposed and demonstrated a novel segmented ring antenna obtained by modifying the regular microstrip-fed dipole radiators taken from the quasi-Yagi shown in Fig. 4 [19]. In our proposed method we have adopted a simple analytical technique in place of these complicated methods, and yet achieved a compact design with a very large bandwidth.

The microstrip-fed quasi-Yagi antenna consists of a half wavelength dipole and an approximately quarter wavelength rectangular director to increase the gain and improve the

front-to-back ratio. The antenna is realized on a high dielectric-constant substrate (0.635-mm-thick and dielectric constant of 10.2 Duroid) with a microstrip feed. The quasi-Yagi employs a truncated microstrip ground plane as the reflecting element, thus eliminating the need for a reflector dipole, resulting in a very compact design. A large bandwidth of 48% a with VSWR < 2 was demonstrated in the X-band. By replacing the dipole and the director of the quasi-Yagi antenna with segmented rings, the bandwidth improved to 120% across the S (2 to 4 GHz) band and the C (4 to 8 GHz) bands. In this work, we present detailed information on the design concept and the development of a wideband segmented ring antenna and split ring antenna, as well as bandwidth and radiation pattern characteristics of each antenna element, and the split ring antenna array.

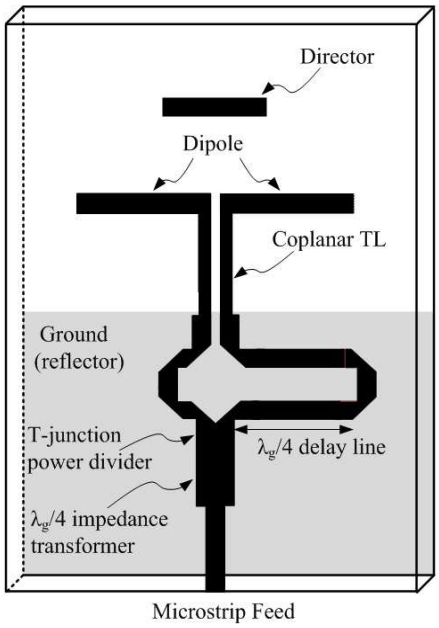

Fig. 4. Schematic of the quasi-Yagi antenna.

CHAPTER 2. THE DEVELOPMENT OF SEGMENTED RING ANTENNA

The wideband characteristic of the spiral antenna makes it an attractive choice where a single antenna is required to send and receive over multiple channels. A wideband channel for an ultra-wideband system, has the potential of high-capacity wireless communication. In our proposed research the characteristics of two arm spirals as radiating elements in the quasi-Yagi antenna area were investigated for wideband potential.

Planar Spiral Antenna

The proposed design was achieved by emulating the two-arm conical spiral antenna [20]. The two-arm conical spiral antenna is constructed by winding a pair of metallic strips around the surface of a truncated cone. Using the same idea, the microstrip-fed spiral antenna was designed in ADS by wrapping metallic traces around the rectangular substrate. This is illustrated in Fig. 5. The significant change in the new design is the replacement of the driver and the director of the quasi-Yagi with spiral elements or spiral arms, with no change in substrate dielectric constant and thickness. The optimized geometry of the feeding system and the size of the spiral elements were determined through an iterative design-and-simulate type of matching using the ADS momentum software. The relative sizes of the antennas are shown in Fig. 6. The spiral antenna is smaller than the quasi-Yagi antenna. The simulated S-parameters of the quasi-Yagi antenna and spiral antenna are shown in Fig. 7. From the plot, it is theoretically proven that the spiral elements can improve the quasi-Yagi's antenna's frequency bandwidth from 48 % (8 - 12 GHz) to 69 % (8-16.5 GHz) for a VSWR ≤ 2.

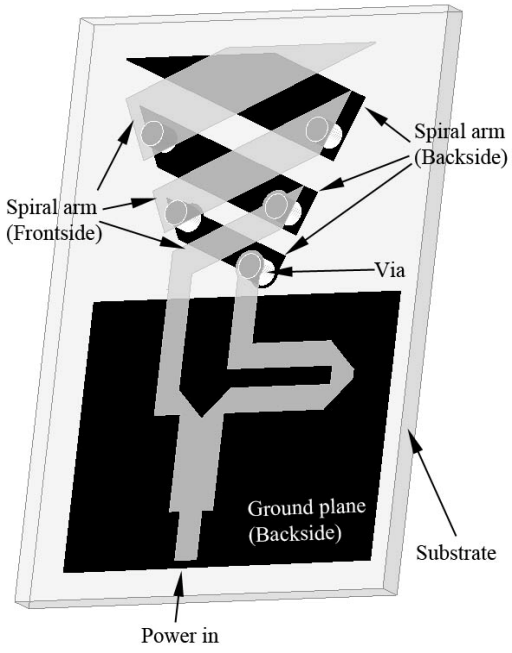

Fig. 5. ADS 3D model planar spiral antenna.

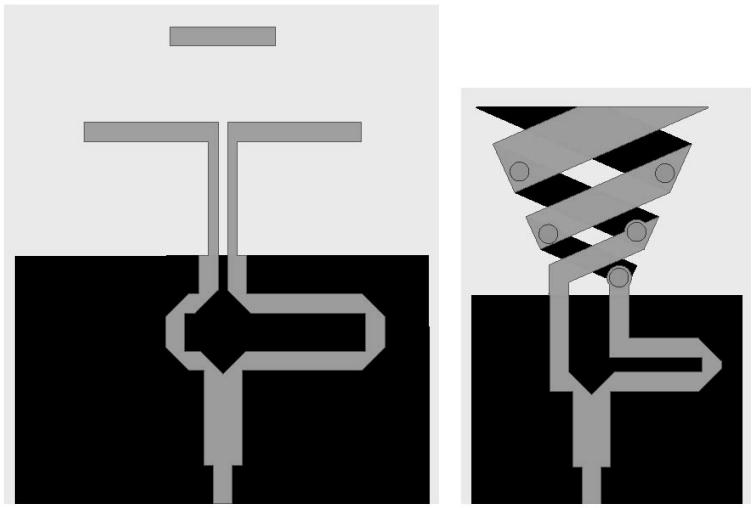

Fig. 6. ADS model planar spiral antenna.

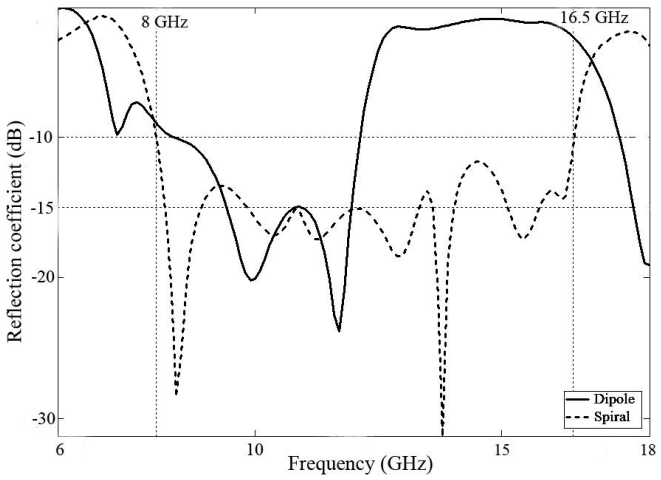

Fig. 7. Simulated reflection coefficients of dipole and spiral antenna.

Segmented-Ring Antenna

The goal is however to achieve a wideband antenna with a bandwidth of 2 - 8 GHz. To achieve this goal, the spiral antenna shown in Fig. 5 was up-scaled by a factor of two and the feeding system [21] shown in Fig. 8 was redesigned for a 5 GHz design frequency using the ADS analytical line impedance tool. From there the final optimized parameters of the segmented ring antenna evolved through iterative design-and-simulate matching using the ADS momentum software until the desired bandwidth was achieved. The design parameter evolutionary process is guided by the bandwidth with a VSWR ≤ 2. The evolved design stages from the spiral antenna to the segmented ring antenna are shown in Figs. 8a through 8d. The simulated S-parameters are shown in Fig. 9.

The up-scaled spiral antenna with vias is shown in Fig. 9a. This antenna achieved a 2.4 GHz bandwidth. Impedance match was difficult to obtain with this design. The physical size of the spiral antenna is much larger than before. Larger via holes relative to signal wavelength are known to present a discontinuity for RF currents, and present parasitic inductances [22], which

may have contributed to the impedance matching problem. One solution to this problem is to reduce the objects or parameters that couple easily, such as the vias and the number of spiral elements, and increase the spacing between the spiral elements on the opposite sides of the substrate. Therefore the substrate thickness was increased from 0.635 mm to 1.27 mm, and the vias were totally eliminated. A thicker substrate with should provide a low impedance capacitive coupling between the spiral element edges. This change resulted in the reduction in the number of spiral elements on each side of the substrate from three to two. The spiral antenna without vias is shown in Fig. 9b. This antenna achieved a 4.4 GHz bandwidth, which is an improvement compared to the previous stage. To further improve the bandwidth, rounded corners were introduced to the antenna elements in Fig. 9b, resulting in the antenna shown in Fig. 9c. This design achieved a 2.6 GHz bandwidth, a degradation of the bandwidth from previous stage. The final change was the conversion of the L-shaped arms in Fig. 9c into the arcs shown Fig. 9d. This change removed unwanted capacitive coupling due to the spiral elements crossing at two places in Fig. 9c. The design in Fig. 9d is called the segmented-ring antenna. It achieved a 5.93 GHz theoretical bandwidth, ranging from 2.25 – 8.18 GHz. The substrate thickness was maintained at 1.27 mm.

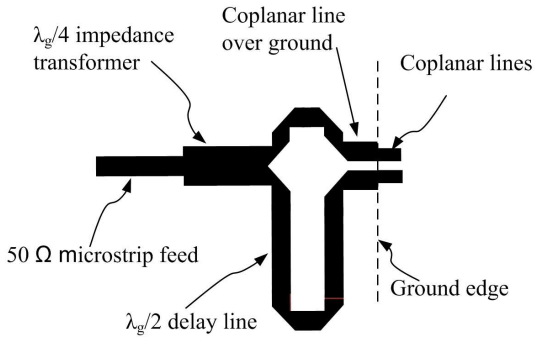

Fig. 8. Feeding system without antenna.

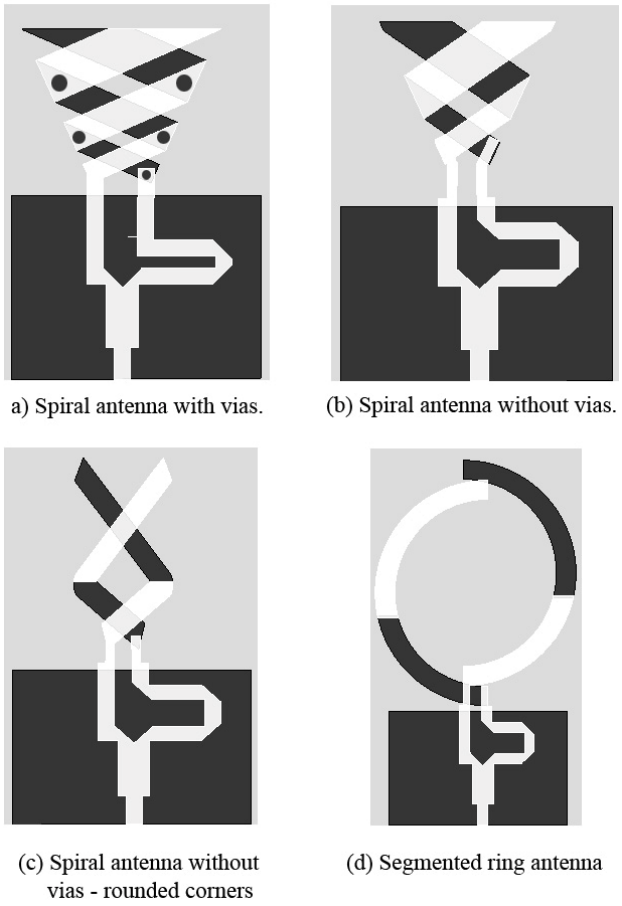

Fig. 9. The evolution of the segmented-ring antenna (exact relative sizes).

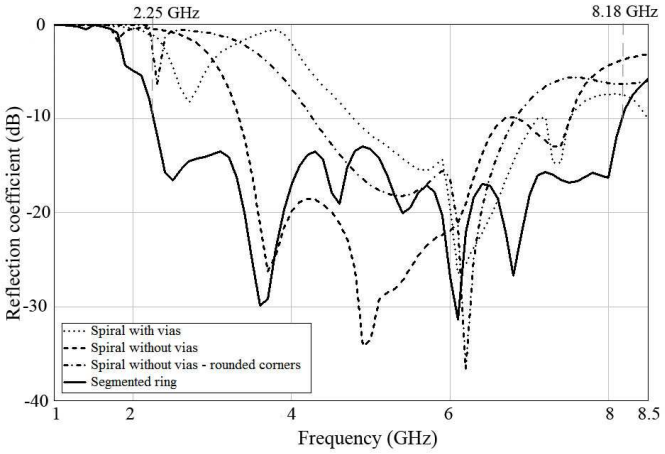

Fig. 10. Simulated reflection coefficients of spiral antennas and segmented-ring antenna.

A rough dimensions for the segmented rings were obtained from an estimate based on the Archimedean spiral antenna. For the Archimedean spiral antenna, the low frequency operating point of the spiral is determined theoretically by the outer radius [23]. Using this concept, the largest arm length (arc) equivalent to the lowest frequency guide-wavelength was calculated. In curved structures such as the spiral or loop antennas, a radiator will be resonant as the perimeter of the curve approaches one wavelength in size. Using this concept the arm length corresponding to the lowest operating frequency (2 GHz) is calculated using

$$\lambda_g = \frac{c}{f\sqrt{\varepsilon_{eff}}} \tag{2}$$

where c is the speed of light in free space, f is the operating frequency, and ε_{eff} is the effective dielectric constant. Using the formula from Pozar, ε_{eff} was determined to be 7.33 [24].

$$\varepsilon_{\text{eff}} = \frac{\varepsilon_{\text{eff}} + 1}{2} + \frac{\varepsilon_{\text{eff}} - 1}{2}\frac{1}{\sqrt{1 + 12\text{d}/\text{W}}} \tag{3}$$

where substrate thickness is d, and conductor width is W. Using (2) , λ_g is 55 mm. The redesigned 50 Ω transmission line width at a 5 GHz center frequency is 1.2 mm. Therefore the initial arbitrary width used for the segmented rings was chosen as 2 mm, a value slightly bigger than line width will provide a good radiating surface.

Fig. 11 shows the layout of the segmented-ring antenna. The antenna is fabricated on a single substrate (1.27-mm-thick Duroid ε_r=10.2 for the S-band and C-band prototype) with segmented rings on both sides. One of the unique features of this antenna is that segmented rings placed on opposite sides of the substrate have no physical contact between them, and there is also no physical contact between the coplanar feed line and the segmented ring A. RF power transfers through capacitive coupling, thus eliminating the need for vias. This greatly simplifies

fabrication complexity. There are four segmented rings, two on each side. The A and C segment pair and the B and D segment pair are equal in length, respectively. Segments A and B are on the backside of the substrate while segments C and D are on the front side of the substrate. During operation, the A and D segments and the C and B segments connect through capacitive coupling formed at their respective junctions.

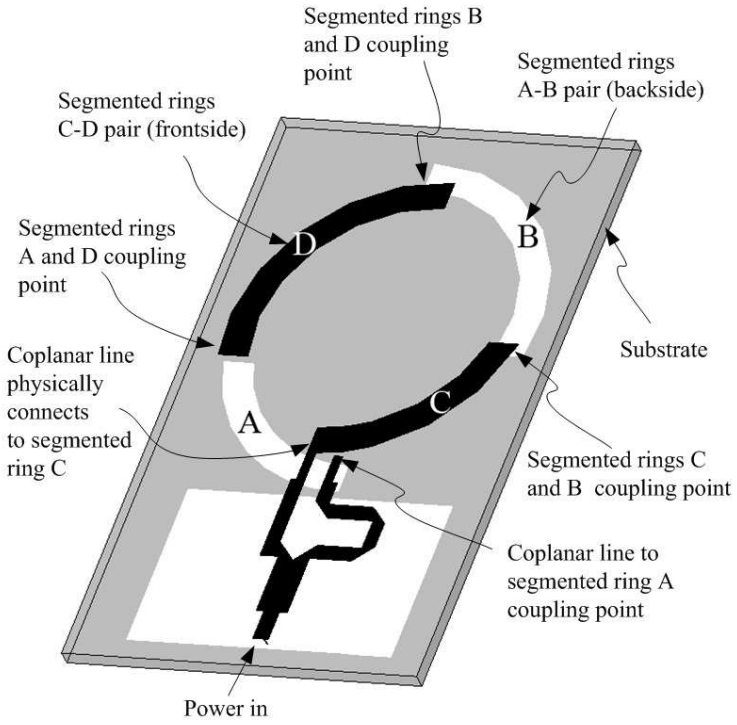

Fig. 11. ADS model of wideband segmented-ring antenna.

Proper design of the segmented ring antenna requires careful optimization of the segmented rings, feeding system, and reflector parameters, which include element spacing, lengths, and widths. This is essential if desirable VSWR characteristics are to be maintained across the entire operating bandwidth. In the segmented-ring antenna, the truncated microstrip ground acts as an impedance-matching parasitic element. The antenna's optimized dimensions

are shown in Fig. 12. The optimized dimensions were arrived through several parameter adjustments. For example, Fig. 13 show how the adjustments of the delay line length, ring width, and right-side-ring position (vertical shifting - up and down) affect the desired bandwidth. The total area of the substrate is approximately 48 mm by 24 mm. A photograph of the S-band and C-band segmented-ring antenna is shown in Fig. 13.

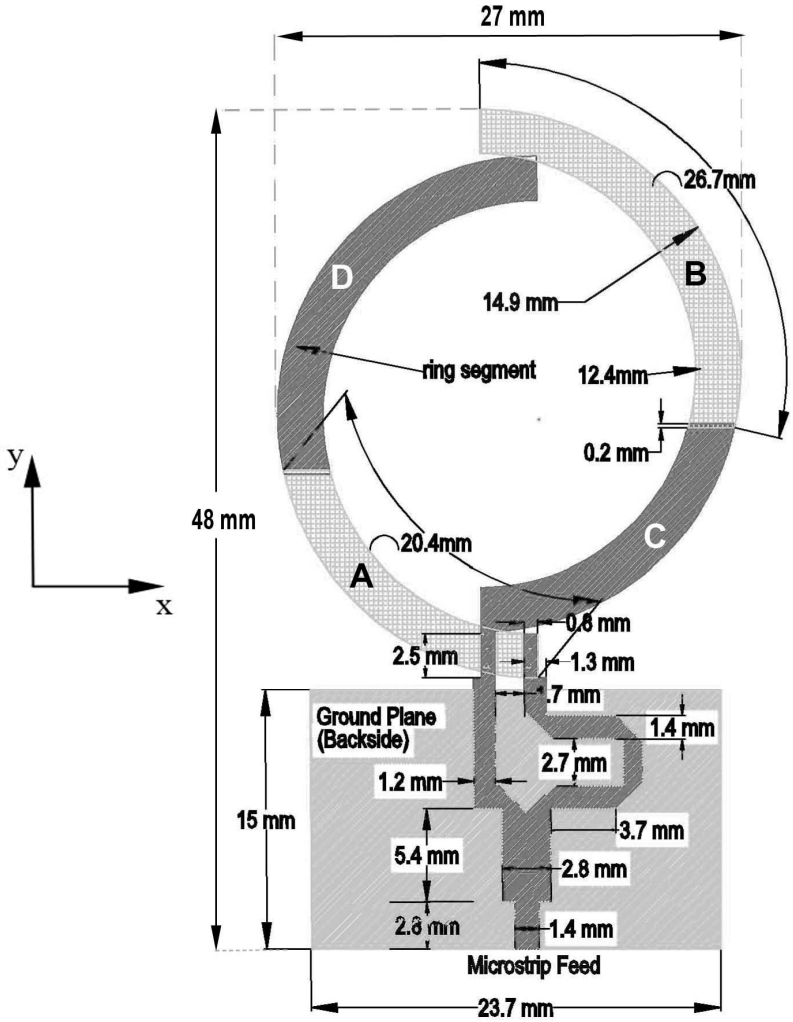

Fig. 12. Schematic of wideband segmented-ring antenna.

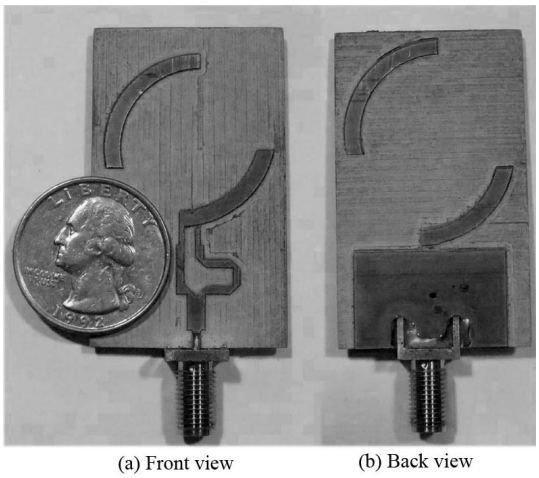

Fig. 13. Photograph of an S-band and C-band segmented-ring antenna.

By choosing the antenna parameters properly, the segmented-ring antenna demonstrates wideband characteristics with modest gains. The simulation in ADS momentum and measured results of the reflection coefficient of the wideband version of the antenna are shown in Fig. 14. The plot also includes the simulation curves of the lumped-element circuit model. A discussion of this model follows in the next section.

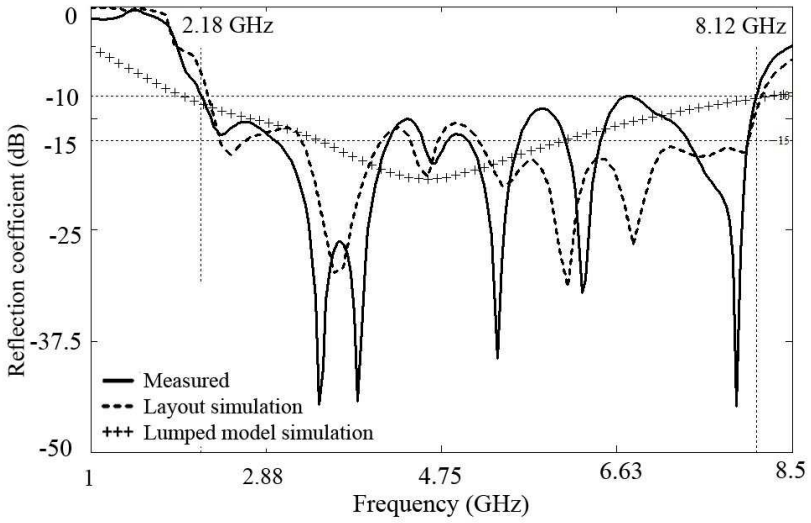

Fig. 14. Lumped-element model, layout and measured S-parameters.

Fig. 15 shows the simulated and measured radiation patterns of both XZ and YZ-cuts. Figs. 15a, 15f, 15i, 15l show the center-fed dipole antenna's analytically computed far-field patterns (E_θ). This pattern was simulated in MathCAD using the derived equation shown in Appendix A. The radiation patterns are stable and broader than the dipole antenna's radiation patterns across the entire frequency band between 2–8 GHz. The radiation patterns have been measured at four different frequencies: 2.5, 4.5, 6.5 and 7.5 GHz, approximately corresponding to the lower end, center, and two upper end frequencies of the operating band of the antenna. The measured radiation patterns of the wideband segmented ring antenna are in close agreement with the simulated patterns. The simulated radiation pattern exhibits nulls at the edges of the substrate. This could be due to the fact that the ADS momentum software uses infinite substrate.

As can be seen, the wideband segmented ring antenna has a broad beam pattern in both planes. The relative gain of the antenna (relative to isotropic) that has been determined through simulation and is shown in Fig. 16. The variation in gain is small across the wide operating bandwidth of the antenna. Since the simulated and measured radiation patterns in both the XZ- and YZ-planes are quite stable and in close agreement across the entire frequency band, the simulated gain in general should have a fair agreement with the actual gain. Nearly omnidirectional patterns have been observed in both the XZ- and YZ-planes in the frequency band of 2-8 GHz. This makes this antenna suitable for many applications such as industrial, scientific and medical (ISM) band and mobile Worldwide Interoperability for Microwave Access (WiMAX) band, satellite-microwave relay. The segmented-ring antenna has a number of advantages over proposed antennas in [10-18]. It has a simple structure for radiating elements, is inexpensive to fabricate, and is easy to integrate with the accompanying electronics. It has

achieved a 120% bandwidth using a simple structure, with the antenna occupying only a substrate that is 48 mm by 27 mm.

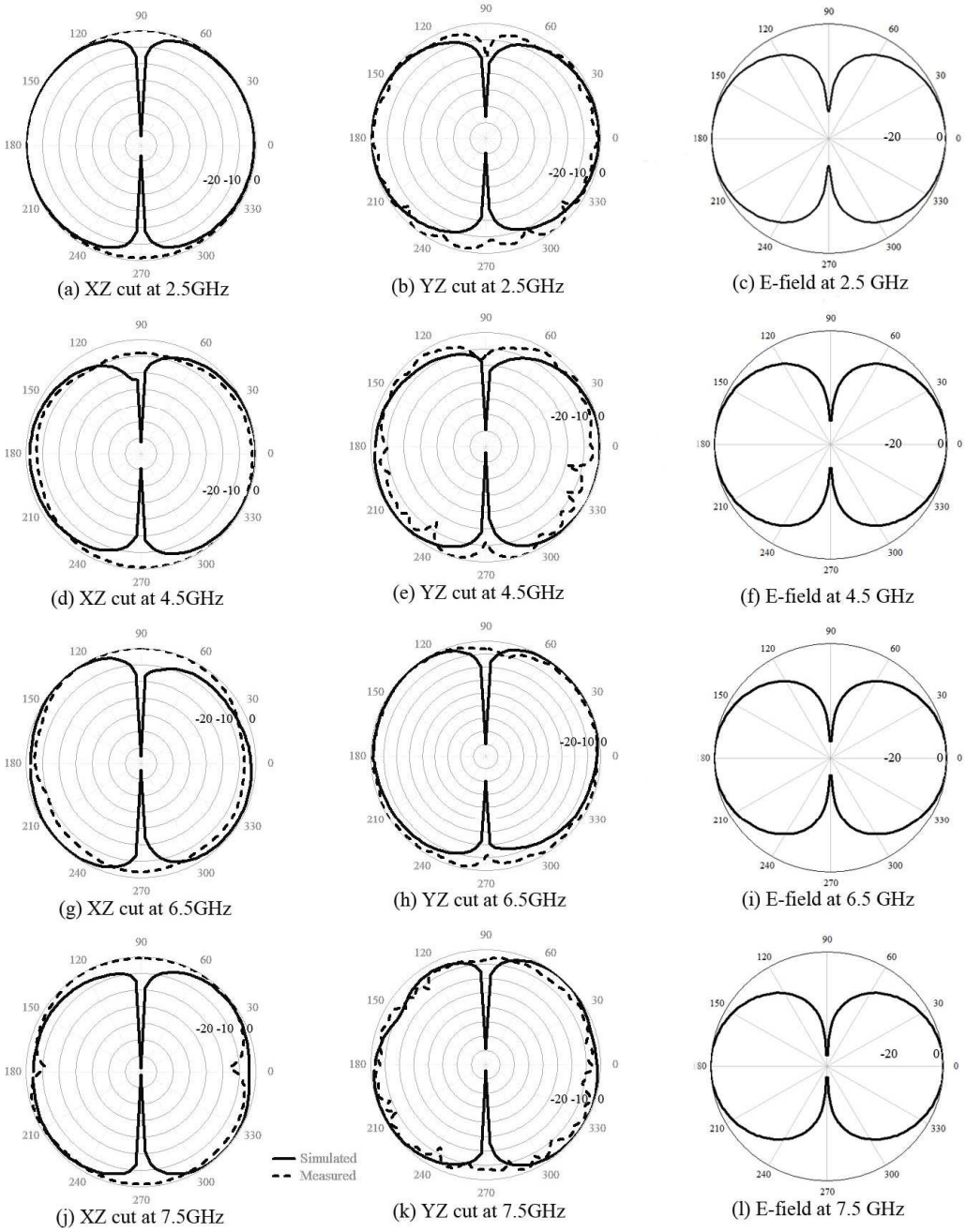

Fig. 15. Measured and simulated radiation patterns of segmented-ring antenna with dipole antenna's analytically computed far-field patterns (c, f, i and l) at 2.5, 4.5, 6.5 and 7.5 GHz.

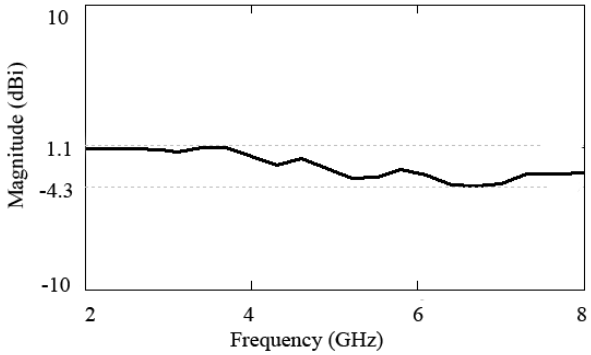

Fig. 16. Simulation of antenna's relative gain along the z-axis.

Circuit Model of Segmented-ring Antenna

To investigate how the segmented-ring antenna widens the bandwidth, a lumped-element circuit model was developed and simulated in ADS. The lumped-element circuit is a convenient way to identify the main parasitic elements that control the antenna's impedance bandwidth. Consider the basic wire half-wave dipole antenna consisting of two straight wires as depicted in Fig. 17a [23]. It is known that a current carrying dipole has inductance (L_1) in series with the parasitic capacitance (C_1), as shown in Fig. 17b. The antenna radiates at resonance; therefore, power dissipation is modeled with the radiation resistance (R_1). The simplified equivalent circuit for a dipole antenna becomes a series RLC network as shown in Fig. 17b. The circuit element values in Fig. 17b assume that the antenna is resonant at 2.7 GHz, with a VSWR ≤ 2 bandwidth of 1 GHz. For simplicity, ohmic resistances, skin effect, coupling between feeds (terminal 1-2), and any other couplings and losses are ignored.

Next, the lumped circuit model developed for the segmented ring antenna is shown in Fig. 18. To understand this model, imagine having two dipole wires bent to form an arc, and connected together at their open ends. Bent-dipole 1 is excited with a source at the input (terminal 1-2), and bent-dipole 2 has capacitance C_{c1} (formed by capacitive couplings

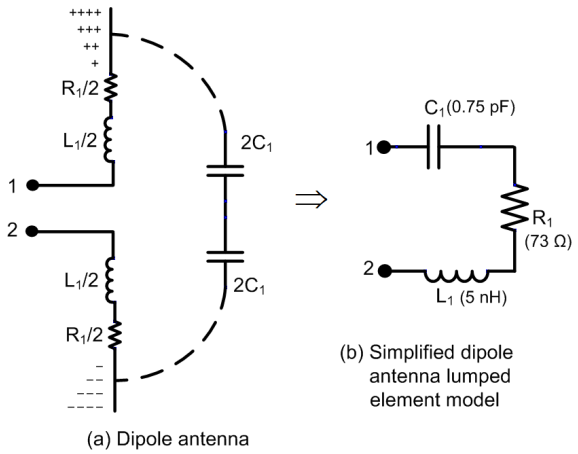

Fig. 17. Dipole antenna model resonating at 2.7 GHz.

between the segmented ring-edges located on the opposite sides of the substrates) at its input (terminal 3-4). $R_1/2$ and $R_2/2$, represent their respective radiation resistances while $L_1/2$, $L_2/2$, C_1 and C_2 are the parasitic elements associated with the respective radiators. The C_c's are the capacitive coupling between segmented rings A and D pair-junction, and C and B pair-junction, respectively. If we further assume that low-impedance couplings are formed by the capacitors (C_c), then these capacitors can be shorted out. However the capacitor C_{c1}, does not qualify for low impedance coupling because the average distance between the edges of the segmented rings B and D is far. This means high impedance capacitance coupling can be formed at junctions B and D and that may affect the input reflection coefficient of the antenna at different frequencies. With these assumptions, Fig. 18 reduces to a simplified model shown in Fig 19. The values used for the parasitics and radiation resistances are estimates used in the ADS simulation. The idea is to compare the bandwidths of the dipole antenna model shown in Fig. 8b with the segmented-ring antenna model shown in Fig 10.

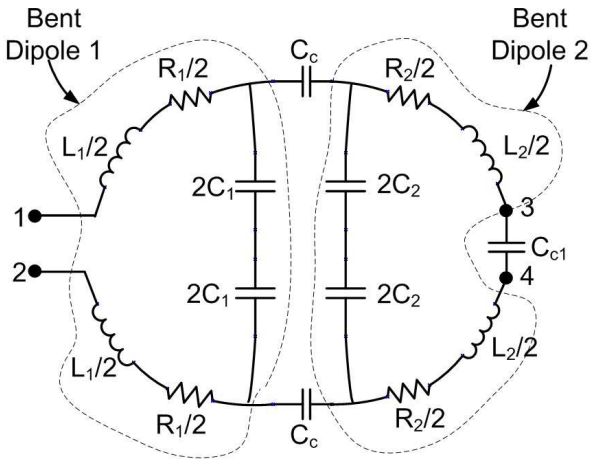

Fig. 18. Segmented ring antenna lumped-element circuit model.

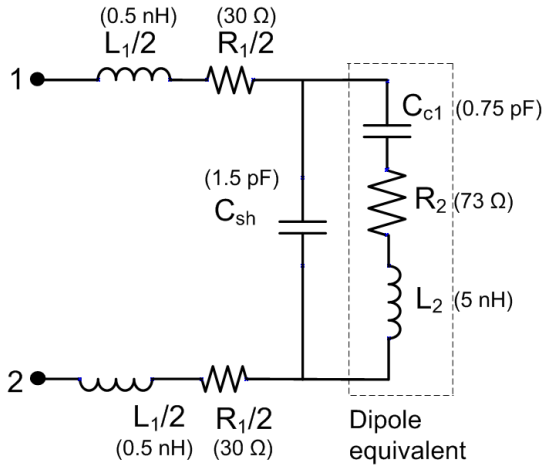

Fig. 19. Simplified segmented-ring antenna lumped-element circuit model.

Fig. 20 shows the lumped-element circuit model simulations. For a VSWR ≤ 2, the simulated segmented ring antenna's bandwidth is 122% while the dipole antenna's bandwidth is only 37%. The simplified segmented ring antenna model in Fig.18 consists of a dipole equivalent part, and additional radiator and parasitic elements (R_1, L_1 and C_{sh}). The segmented ring antenna therefore has created additional parasitics that serve as wideband matching network elements, responsible for increasing the bandwidth.

The effect of varying the series inductance ($L_1/2$) and shunt capacitance (C_{sh}) was investigated through simulation in ADS. The results are shown in Fig. 21 and Fig. 22 respectively. First, with C_{sh} held constant, a decrease in $L_1/2$ below the nominal value (0.5 nH) passes high-frequency signals, while an increase in $L_1/2$ blocks high-frequency signals. Next, with $L_1/2$ held constant, an increase in the C_{sh} blocks high frequency signals, but passes low-frequency signals. A decrease in C_{sh} does the opposite. The shunt capacitance doesn't quite increase the bandwidth but shifts the passband to the lower frequency range at a higher C_{sh} value and vice versa at a lower C_{sh} value. An equation to validate the input impedance of the simplified segmented-ring circuit model was derived as shown in (4), and the magnitude of the input impedance, real part of the input impedance, imaginary part of the input impedance and the input reflection coefficient are plotted in MathCAD as shown Fig. 23 (a through d).

$$Z_{in} = j\omega L_1 + R_1 + \frac{R_2 + j\left[\omega L_2 - \frac{1}{\omega C_{c1}}\right]}{1 + \frac{C_{sh}}{C_{c1}} - \omega^2 L_2 C_{sh} + j\omega C_{sh} R_2} \tag{4}$$

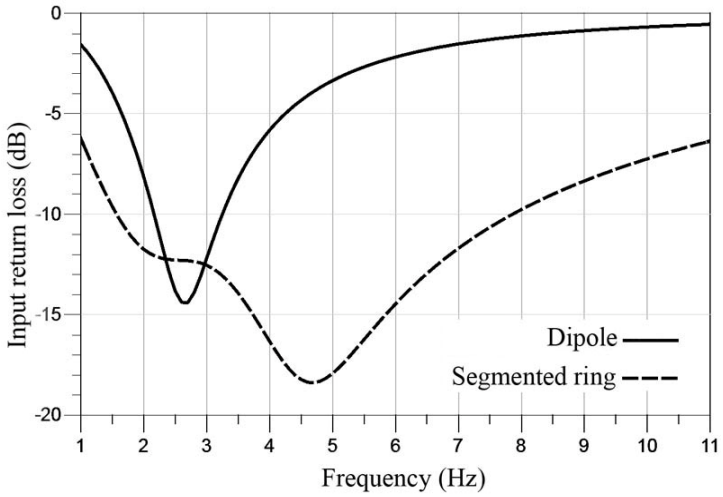

Fig. 20. Lumped-element circuit model reflection coefficients.

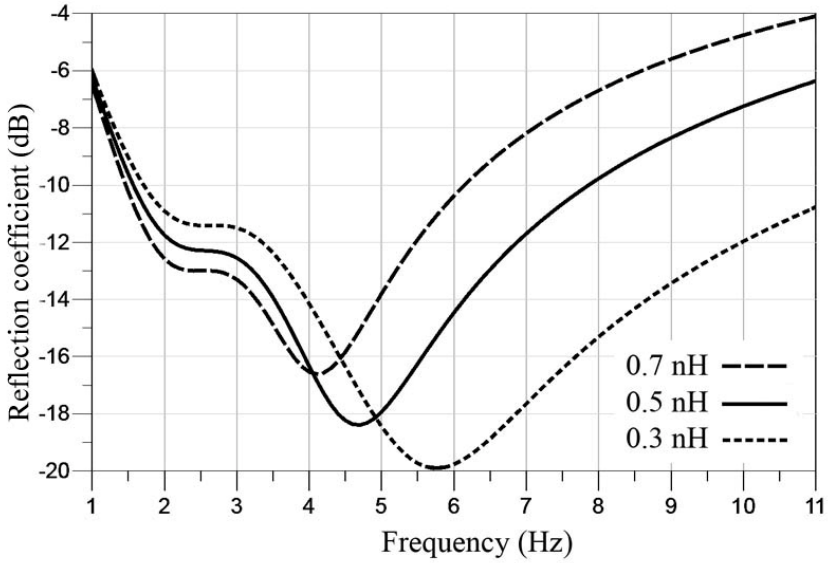

Fig. 21. Segmented ring lumped-element circuit model reflection coefficients for various series inductor ($L_1/2$) values.

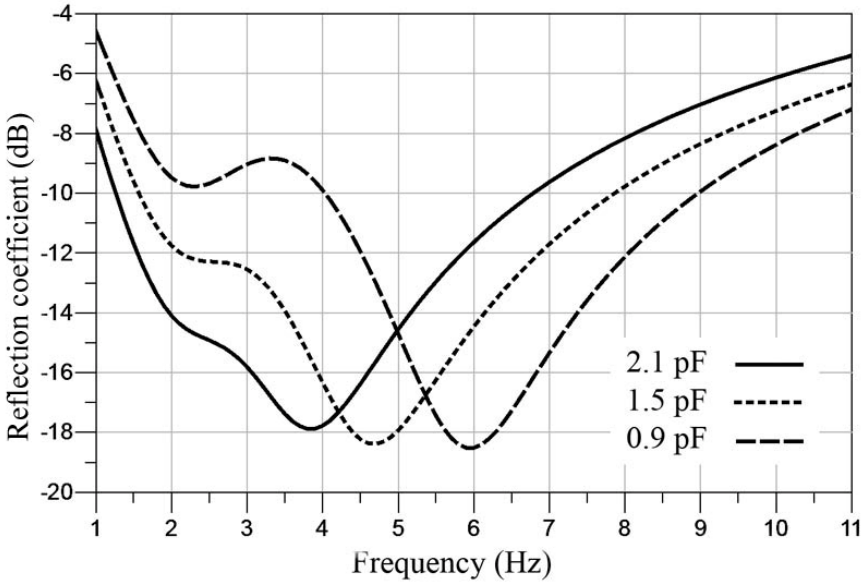

Fig. 22. Segmented ring lumped-element circuit model reflection coefficients for various shunt capacitor (C_{sh}) values.

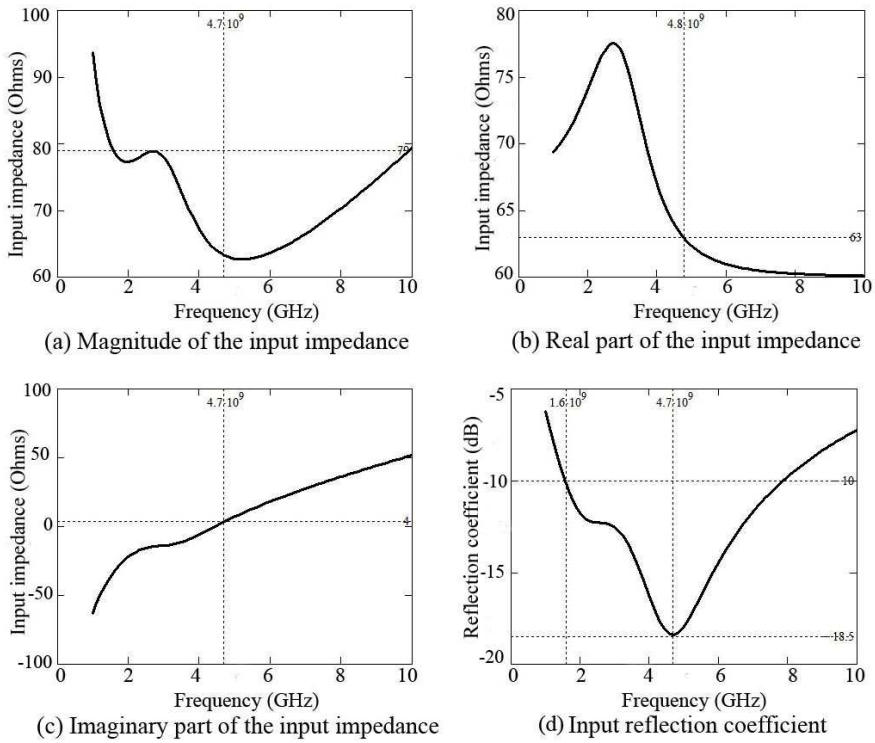

Fig. 23. Segmented-ring: (a) Magnitude of the input impedance (b) Real part of the input impedance (c) Imaginary part of the input impedance (d) Input reflection coefficient.

Design and Analysis of the Segmented-ring Antenna

The simulated reflection coefficient curve in Fig. 14 indicates good impedance matching at some frequencies (dips in the simulated reflection coefficient curve), which are regarded as the resonances of the antenna [25]. The first resonance occurs at around 2.5 GHz, the second, third, fourth, fifth, sixth, seven and eight resonances occurs at 3.6 GHz. 4.55 GHz, 5.4 GHz, 6.1 GHz, 6.8 GHz, 7.6 Hz and 7.95 GHz respectively. It is evident that the resonances, which are closely distributed across the spectrum, result in a wideband -10 dB bandwidth [25].

Figs. 24 to 26 illustrate the parameter changes for the antenna that have contributed to the multiple resonances. In order to investigate the effects of some design parameters, one parameter at a time was adjusted in ADS, and the resulting reflection coefficients were observed.

It is evident from Figs. 24 to 26 that the performance is quite sensitive to the feed gap *h*, the ring width, the delay line length, and the segmented-rings' mean radius.

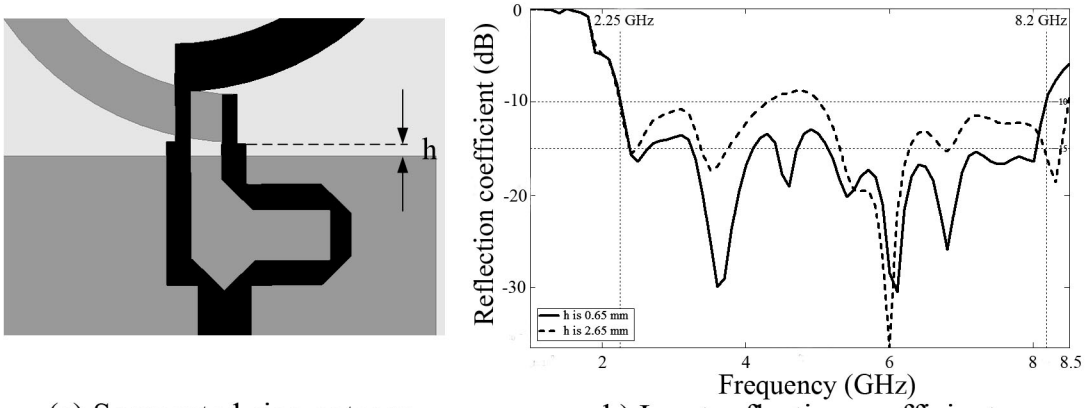

(a) Segmented-ring antenna b) Input reflection coefficients

Fig. 24. Segmented-ring antenna's reflection coefficient at feed gaps: h = 0.65 and h=2.65 mm.

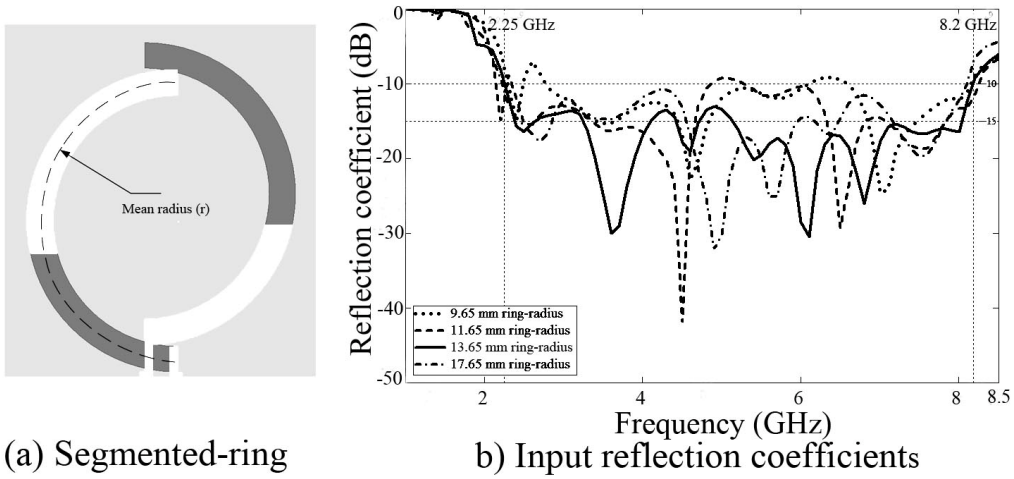

(a) Segmented-ring b) Input reflection coefficients

Fig. 25. Segmented-ring antenna's reflection coefficient for different mean ring radii.

In order to gain further insight into the antenna operation, the animation of surface current variation at different resonances was generated and observed in ADS. Figs. 27a, 27b and 27c show the snapshots of the surface current patterns at three resonant frequencies (2.5 GHz, 4.55 GHz and 7.95 GHz) during the first-half cycle of the RF signals. At the first resonance (2.5 GHz) the current is flowing in the clockwise direction on three of the segmented-rings,

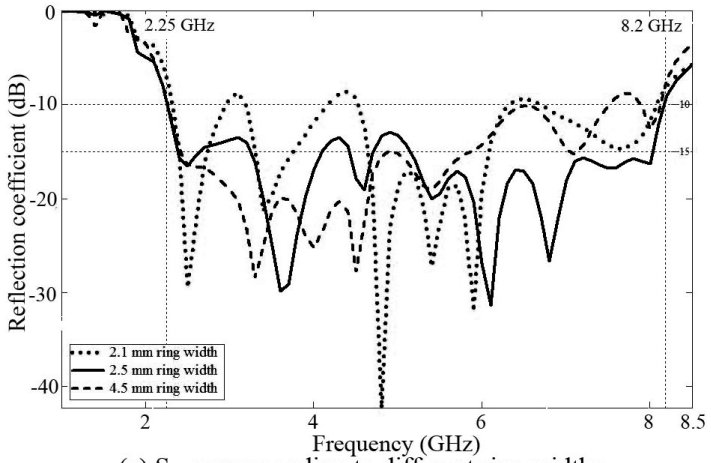

(a) S_{11} corresponding to different ring widths

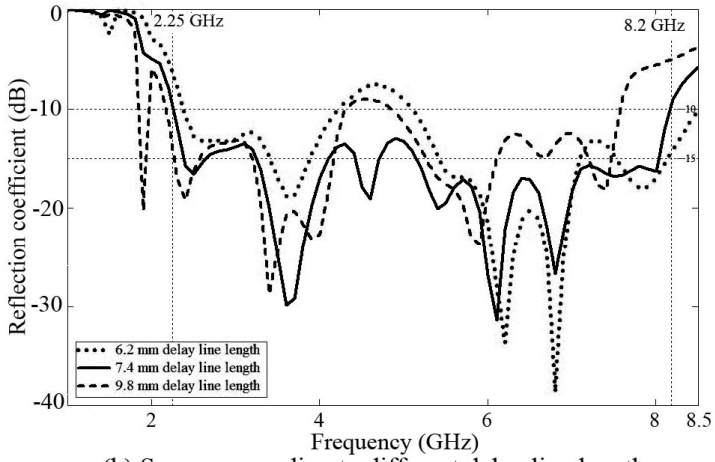

(b) S_{11} corresponding to different delay line lengths

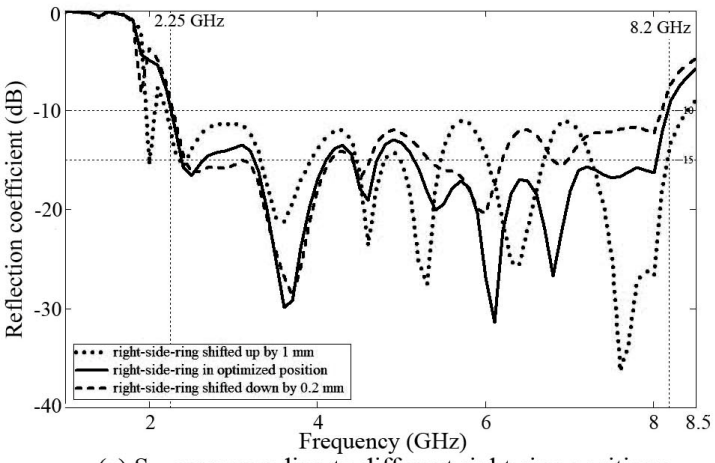

(c) S_{11} corresponding to different right-ring positions

Fig. 26. Segmented-ring antenna parameter adjustment and the corresponding reflection coefficients.

occupying approximately 78% of the ring area. The net current direction is clockwise, and that determines the far-field radiation strength and pattern during the first-half cycle. At 4.55 GHz and 7.95 GHz, it appears that some of the surface current is in the clockwise direction and some in the counter clockwise direction. That may be the reason why the simulated gain (dBi) along the z-axis is better near the lower frequency end than at the higher frequency end (Fig. 16). However, there must be a net current direction to contribute to the far-field radiation, and ADS is not able to capture the current direction well at higher resonant frequencies. This is because of the capacitive elements (capacitive coupling through the dielectric) around the antenna. The capacitive element presents a delay to the RF surface currents. However, the surface current direction and distribution for the split-ring antenna is distinct as show in Fig. 36 (page 40, Chapter 3). This is so because of the reduction in the number of the capacitive elements, such as the via-less connections. During the first resonance (2.1 GHz) the clockwise-current occupies the entire surface area of the split-ring, at 4.5 GHz the clockwise-current occupies about 80% of the split-ring area, and at 7.5 GHz, half of the surface current is in the clockwise direction and the other half in the counter-clockwise direction.

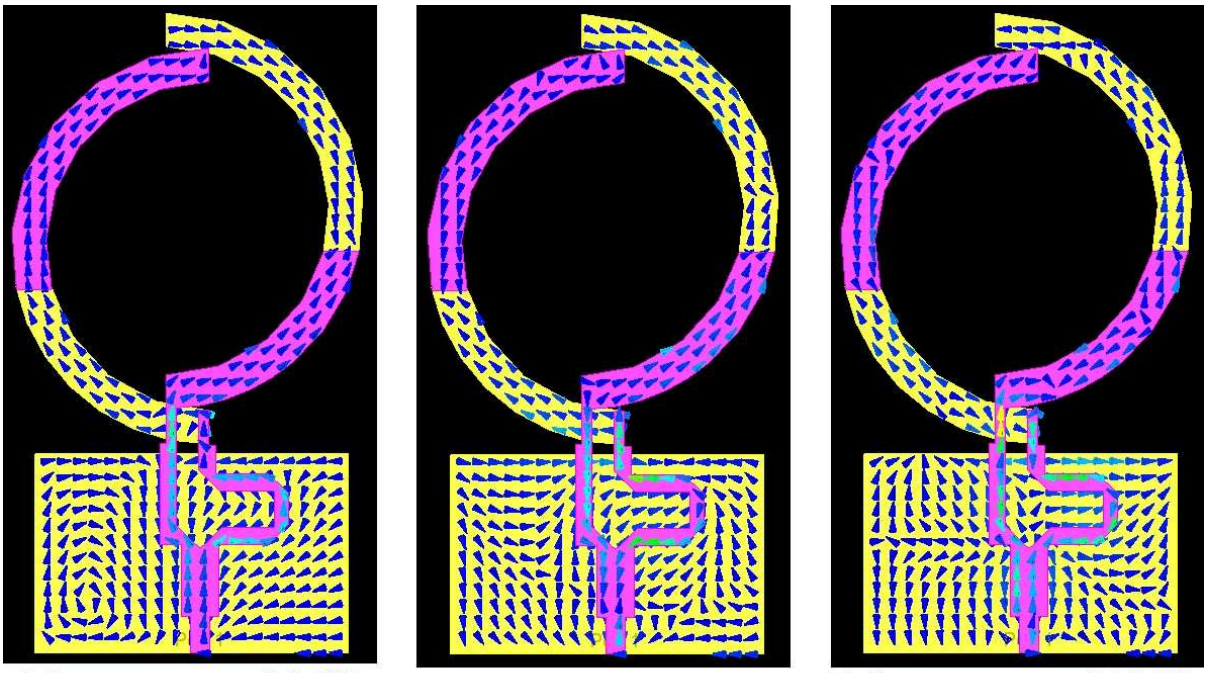

(a) Current pattern at 2.5 GHz (b) Current pattern at 4.55 GHz (c) Current pattern at 7.95 GHz

Fig. 27. Segmented-ring antenna surface current patterns for 2.5, 4.55 and 7.95 GHz.

Conclusion – Segmented-ring Antenna

Experimentally the antenna demonstrated a bandwidth of 120% for a VSWR ≤ 2, and simulated gain between -4.3 to 1.1 dBi. This is more than twice the bandwidth of the quasi-Yagi antenna. The lumped-element model analysis revealed that the segmented-ring antenna has introduced parasitic elements (L_1 and C_{sh}), that are responsible for increasing and controlling the passband of the antenna and making it resonant (VSWR < 2) at a wide range of frequencies. The right amount of inductive reactance combined with the right amount of capacitive reactance make up a tuned circuit to either pass or not pass some frequencies. By careful optimization of the segmented rings, ground plane, and the spacing between the feeds, the amount of parasitics can be altered to achieve the desired bandwidth. The antenna achieved a 2-8 GHz bandwidth and is suitable for many applications such as the wireless local area network (WLAN) and mobile

WiMAX or satellite-microwave relays. The result shows that segmented rings are another promising way for enhancing bandwidth. The next chapter presents the split-ring antenna, which evolved from the segmented-ring antenna.

CHAPTER 3. SPLIT-RING ANTENNA

The split-ring antenna is a design derived from of the segmented ring antenna. The split ring antenna uses the same dielectric-constant substrate (1.27-mm-thick ε_r = 10.2 Duroid) as the segmented ring antenna with a microstrip feed. This antenna also achieved a large operational bandwidth of 120 % for VSWR $\leq$ 2 in the S and C bands. The total area of the substrate is approximately 39 mm by 26 mm. The motivation for developing the split-ring antenna is to design a more compact and efficient antenna for array applications since it was difficult to design an array using the segmented ring antenna. Impedance matching of the transmission line to the segmented-ring antenna array is a challenging task. Excessive mutual coupling between array elements may have changed the input impedance of each antenna element, which in turn affected the overall input impedance of the array. Implementing a matching network will increase array size and design complexity, and the impedances of the elements also change due to undesired coupling. Thus, the matching network solution is not viable. On the other hand the source of excessive mutual coupling should be addressed. In other words, the segmented rings can be redesigned to lower the possible excessive mutual couplings in a array environment. The excessive mutual coupling in the segmented-ring antenna arrays may have occurred due to the via-less transmissions, causing an antenna-effect that couples onto an adjacent antenna elements thus changing its radiation properties. Another potential problem with this design is that the energy transfer through capacitive coupling can be subjected to stored energy, excessive fringing fields, or energy dissipation within the substrate (dielectric loss), and present discontinuity to the smooth flow of surface currents. Trapped electromagnetic energy along the surface of the substrate leads to the generation of surface waves. The power launched into the surface waves is

power which will eventually be lost; hence the excitation of surface waves lowers the overall radiation efficiency of the antenna [26, 27]. Parameters controlling the level of mutual coupling are: the element spacing, the relative placement and the radiation pattern of the elements [28]. Mutual coupling is an important phenomena between elements within an array environment, which may not only complicate the array design, but also cause scan-blindness in planar antenna arrays. All these phenomena will affect the input impedance of the elements and the elements' radiation patterns [19, 28, 29]. If segmented rings are affected by one or more of the above mentioned phenomena, then that may cause complications in the array environment. Moreover, the antenna-effect at via-less terminals can aggravate the affects of these phenomena. To verify this, an alternate design called a "split-ring" antenna is designed and compared with the segmented-ring antenna's performance. The split-ring antenna has several advantages over the segmented-ring antenna. First, the realized split-ring antenna eliminated all the via-less capacitive couplings. Secondly, a broader radiation pattern with more stable gain is achieved. The net result is that all radiator elements are moved to the top side of the substrate. The antenna is implemented on the same dielectric substrate material and thickness with a microstrip feed occupying a smaller area compared with the segmented-ring antenna.

Split-ring Antenna Design

The antenna is fabricated on a single substrate (1.27-mm-thick Duroid for the S-band and C-band prototype) with split-rings. Unlike the segmented-ring antenna, the radiators of this antenna lie on the top side of the substrate. The ADS model of the wideband split ring antenna is shown in Fig. 28. In the split-ring antenna, the truncated microstrip ground acts as an impedance matching parasitic element. The antenna's optimized dimensions are shown in Fig. 29. A

photograph of the S-band and C-band split-ring antenna is shown in Fig. 30. Fig. 31 shows the relative size of the split ring antenna with respect to the segmented ring antenna. Proper design of the split ring antenna requires careful optimization of the split rings, feeding system, and ground plane parameters, which includes element spacing, lengths, and widths. This is essential if desirable VSWR characteristics are to be maintained across the entire operating band. By choosing the antenna parameters properly, through design and optimization in ADS, the split-ring antenna demonstrates a 119 % bandwidth for a VSWR ≤ 2. The simulation in ADS momentum and the measured reflection coefficients of the wideband version of the antenna is shown in Fig. 32.

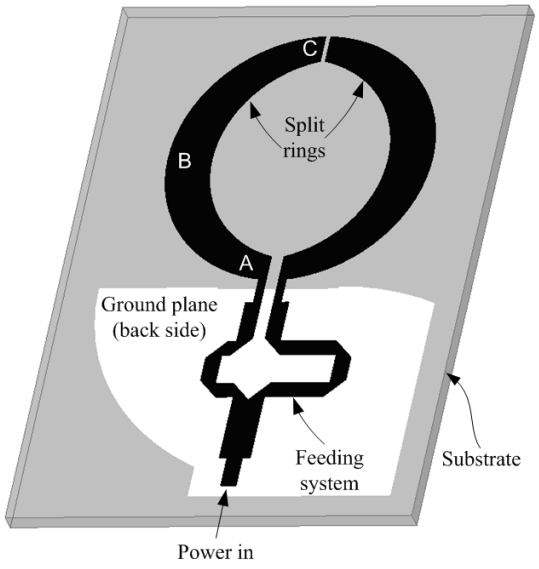

Fig. 28. ADS model of wideband split-ring antenna.

Fig. 33 shows the simulated and measured radiation patterns of both the XZ and YZ cuts. The radiation patterns are stable across the entire frequency band between 2 – 8 GHz. The radiation patterns have been measured at four different frequencies: 2.5, 4.5, 6.5 and 7.5 GHz, approximately corresponding to the lower end, center, and two upper end frequencies of the

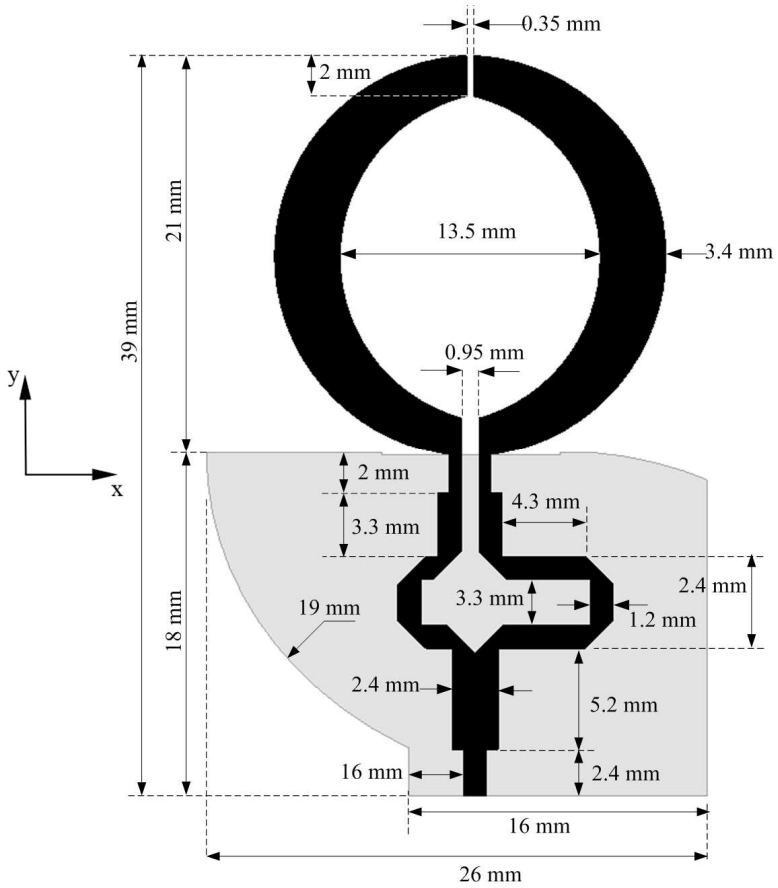

Fig. 29. Schematic of wideband split-ring antenna.

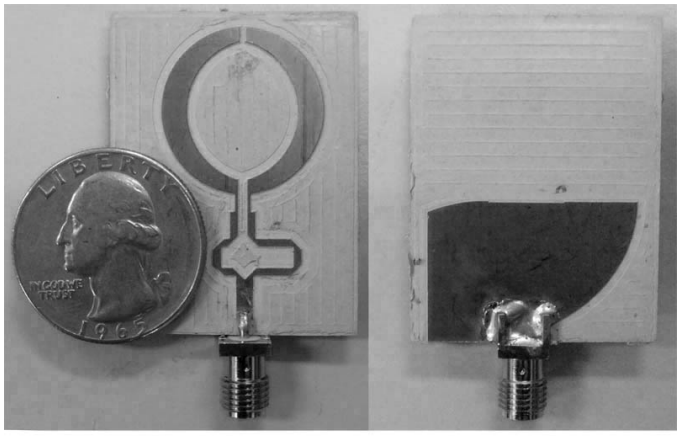

(a) Front view (b) Back view

Fig. 30. Photograph of an S-band and C-band split-ring antenna.

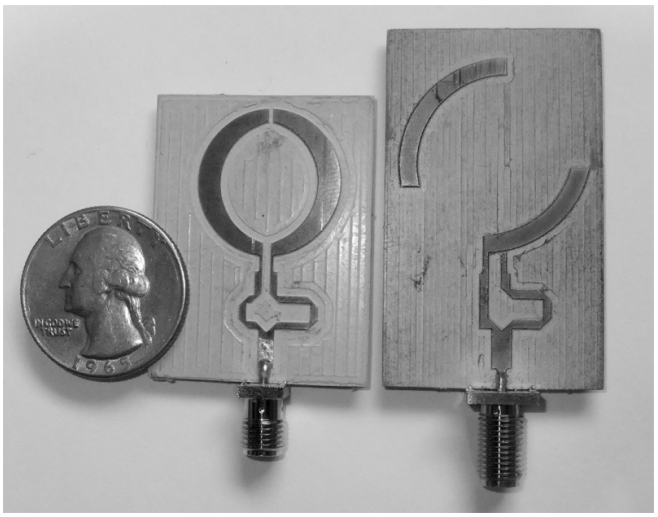

Fig. 31. Photograph of split-ring antenna and segmented-ring antenna.

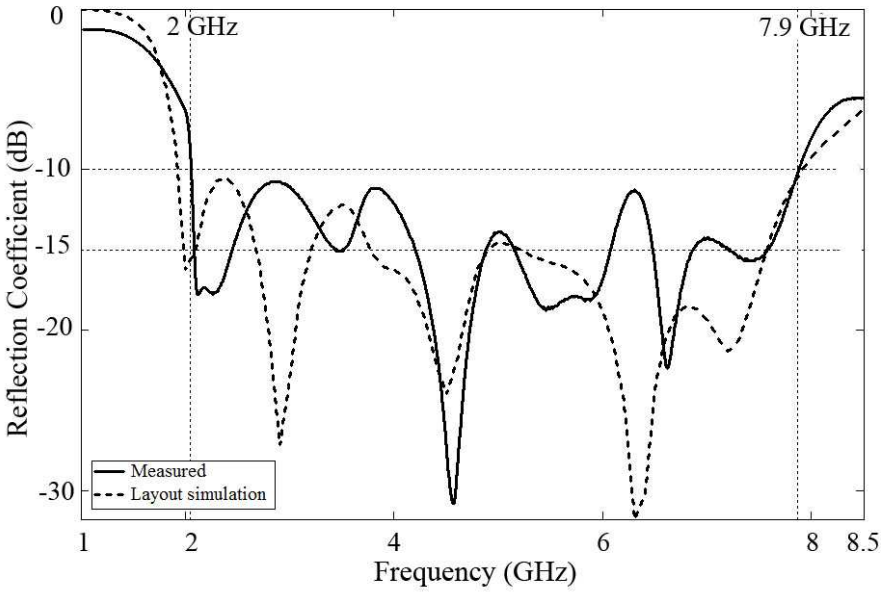

Fig. 32. Simulation and measured input reflection coefficient of the prototype split-ring antenna.

operating band of the antenna. The measured radiation patterns of the wideband segmented ring antenna are in close agreement with the simulated patterns. Fig. 34 shows a comparison of the measured radiation patterns of the split-ring antenna with the segmented-ring antenna. It can be seen that the split-ring antenna has a comparable or broader beam patterns than the segmented-

ring antenna. A comparison of simulated relative gains (dBi) of the antennas is shown in Fig. 35. The figure indicates that the split-ring antenna's gain is more stable over the operating band. Since the simulated and measured radiation patterns in both the XZ and YZ-planes are quite stable and in close agreement across the entire frequency band, the simulated gain in general should have a reasonable agreement with the actual gain. Nearly omnidirectional patterns have been observed in both the XZ and YZ-planes in the frequency band 2- 8 GHz. This makes this antenna applicable for many applications where a more area coverage is needed.

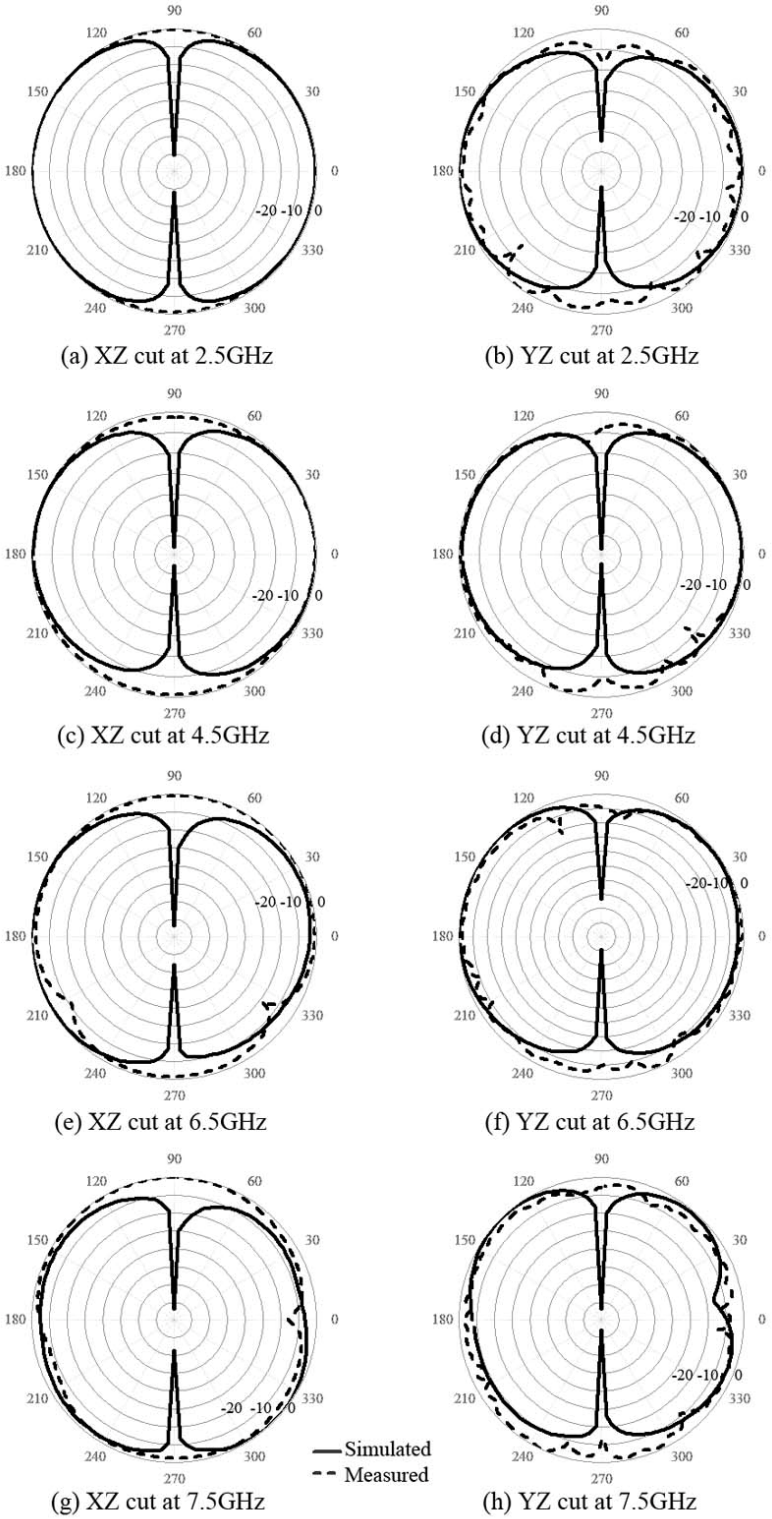

(a) XZ cut at 2.5GHz (b) YZ cut at 2.5GHz

(c) XZ cut at 4.5GHz (d) YZ cut at 4.5GHz

(e) XZ cut at 6.5GHz (f) YZ cut at 6.5GHz

(g) XZ cut at 7.5GHz (h) YZ cut at 7.5GHz

Fig. 33. Measured and simulated radiation patterns of split ring antennas at 2.5, 4.5, 6.5 and 7.5 GHz.

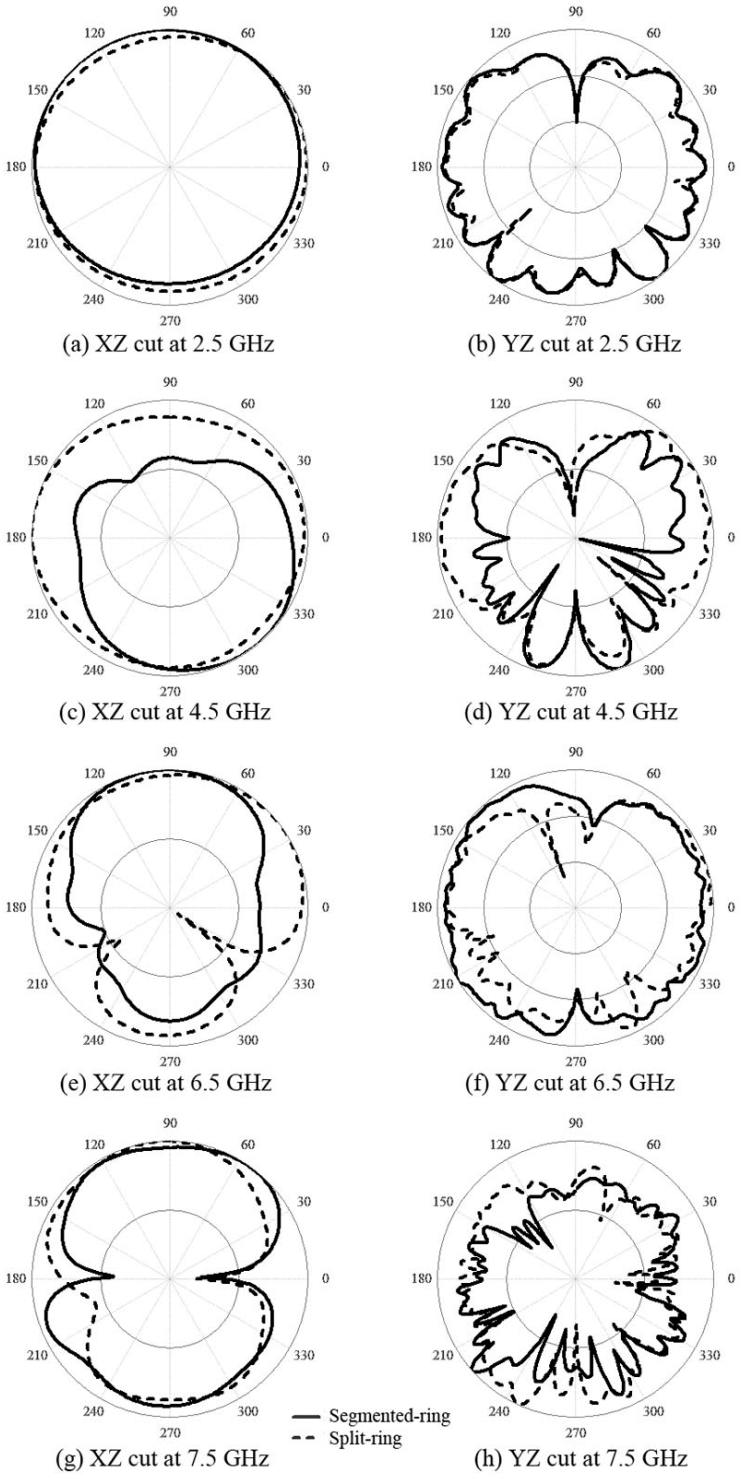

(a) XZ cut at 2.5 GHz (b) YZ cut at 2.5 GHz

(c) XZ cut at 4.5 GHz (d) YZ cut at 4.5 GHz

(e) XZ cut at 6.5 GHz (f) YZ cut at 6.5 GHz

(g) XZ cut at 7.5 GHz (h) YZ cut at 7.5 GHz

Fig. 34. Measured radiation patterns of split-ring and segmented –ring antennas at 2.5, 4.5, 6.5 and 7.5 GHz.

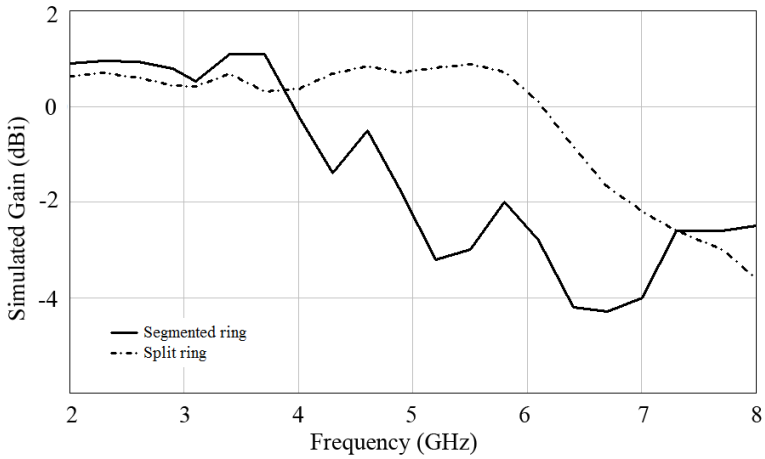

Fig. 35. Simulation of antenna's relative gain along the z-axis.

Circuit Model of Split-ring Antenna

The lumped element circuit model used for segmented ring antenna can be used for the split-ring antenna too. Referring to the split-ring antenna shown in Fig. 18, the capacitor coupling (Cc) is shorted out because the ring at point 'B' is not segmented anymore but a continuous metal. The coupling capacitor Cc1 at point 'C' remains because of the open ended split-rings. This simplifies to the same model used for segmented-ring antenna shown in Fig. 19.

Split-ring Layout Design

The antenna design and optimization of the split-rings and feeding system has been carried out using ADS momentum software. Initial layout parameters were obtained from the segmented ring antenna, then ADS momentum software was used to re-design the entire metallic structure. The four segmented rings are replaced with two identical segmented rings called split rings. The geometric sizes and shapes of the dimension were determined through iterative design-and-simulate matching with the ADS momentum software. Fig. 28 shows the physical layout of the split ring antenna. At the ends (points A and C), the widths are the same. In the middle section of the split-ring antenna (point B), the radiator's width is wider than the ends.

Basically, the shape and size of the split-rings, spacing between the coplanar lines, delay line length, and the shape and size of the ground plane contribute to the simulated and measured bandwidths of 119% (for the split-ring antenna) and 120% (for the segmented ring antenna), respectively for a VSWR ≤ 2.

Design and Analysis of the Split-ring Antenna

The split-ring antenna is an upgraded version of the segmented-ring antenna. As shown in Fig. 32 (simulated reflection coefficient), the first resonance occurs at around 2 GHz, the second, third, fourth and fifth resonances occur at 2.9 GHz. 4.5 GHz, 6.3 GHz and 7.2 GHz, respectively. It is evident that these resonance modes, which are closely distributed across the spectrum, result in a bandwidth at -10 dB that is substantial [25].

The split-ring antenna eliminated all the capacitive elements formed through the dielectric. Thus the delay presented to the RF surface currents is reduced. It is evident from Fig. 36 that the net surface current direction and distribution is well defined. That may be the reason why the split-ring antenna's relative gain (dBi) along the z-axis is more stable and higher than that of the segmented-ring antenna (Fig 35).

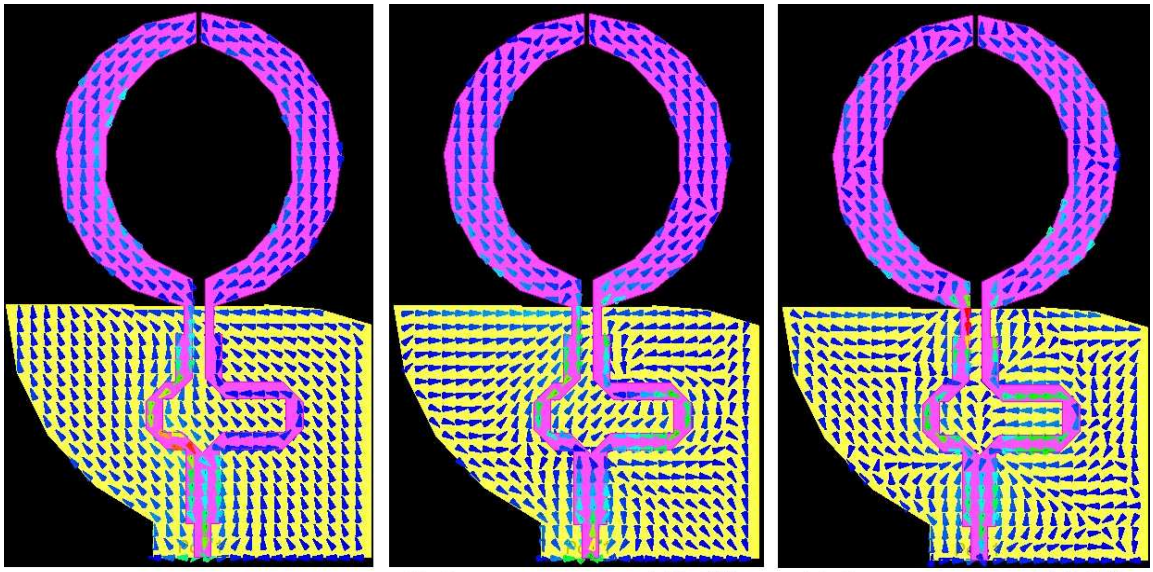

(a) Current pattern at 2.1 GHz (b) Current pattern at 4.50 GHz (c) Current pattern at 7.5 GHz

Fig. 36. Split-ring antenna surface current pattern 2.1, 4.5 and 7.5 GHz.

CHAPTER 4. DIPOLE ANTENNA ARRAY

This chapter presents the design and analysis of a four-element dipole antenna arrays using ADS simulation. The idea is to show the art of designing antenna array by using a simple microstrip dipole antenna model. Array design using a dipole antenna that has a known radiation pattern will provide more insight into the impedance matching technique and radiation pattern analysis. This exercise is essential before moving on and designing arrays using the new split-ring antenna element.

Dipole Antenna Array Design

This section demonstrates the design and simulation of a microstrip dipole antenna array in the frequency range of 8 to 12 GHz. The quasi-Yagi is basically a standard dipole with a quarter wavelength director [19]. The quasi-Yagi antenna design can be easily converted to a regular dipole antenna by removing the director. The resulting dipole antenna is shown in Fig. 37a, and Fig. 37b and Fig 37c show the XZ-cut radiation pattern, and the input reflection coefficient respectively.

Usually the radiation pattern of a single-element antenna is relatively wide, i.e., it has relatively low directivity (gain). In long distance communications, antennas with high directivity are often required. Such antennas are possible to construct by enlarging the dimensions of the radiating aperture (maximum size much larger than λ). This approach however may lead to the appearance of multiple side lobes. Besides, the antenna is usually large and difficult to fabricate [30]. Another way to increase the electrical size of an antenna is to construct it as an assembly of radiating elements in a proper electrical and geometrical configuration – antenna array, as shown in Fig. 38 (a,d and g). These array elements are made identical for simpler design and

fabrication. The total field of an array is a phasor superposition of the fields radiated by the individual elements. To provide a directive pattern, the partial fields (generated by the individual elements) interfere constructively in the desired direction and interfere destructively in the remaining space. The overall antenna pattern is controlled by the geometrical configuration of the overall array (linear, circular, spherical, rectangular, etc.), the relative placement of the elements, the excitation amplitude of the individual elements, the excitation phase of each element and the individual pattern of each element. Directivity is a factor that describes how well an antenna focuses electromagnetic energy in a given direction. A dipole transmits or receives most of its energy perpendicular to the surface of the antenna, while little energy is transferred along them [31]. Arrays are usually electrically large and have better directivity than a single-element antenna [31]. Since their directivity is large, arrays can capture and deliver to the receiver a larger amount of power. This is demonstrated using a four-element array radiation pattern shown in Fig 38b. Figure 38b shows that with no increase in power from the transmitter, the amount of radiation in a given direction would be greater. Since the input power has not increase, this increased directivity is achieved at the expense of gain in other directions. In many applications, sharp directivity is desirable although no need exists for added gain. Also demonstrated in Fig. 38e and 38h, is the main broadside beam can be tilted at different angles. Such arrays are usually referred to as scanning arrays.

In Fig. 38e a tilted-beam angle of 6 degrees is achieved using meandering lines. Embedding phase shifting in the power divider itself doubles the scan angle to 12 degrees (Fig. 38h). When the number of elements is doubled, the directive gain increases further, as shown in Fig. 39. Thus by arranging dipole elements with linear spacing, the performance and

effectiveness of the dipole could be greatly increased and the pattern of the dipole RF energy could be "beamed" or focused in one direction. The net effect is making it appear as if the array as array has amplified the power, yielding much stronger signals both on receive and transmit [32].

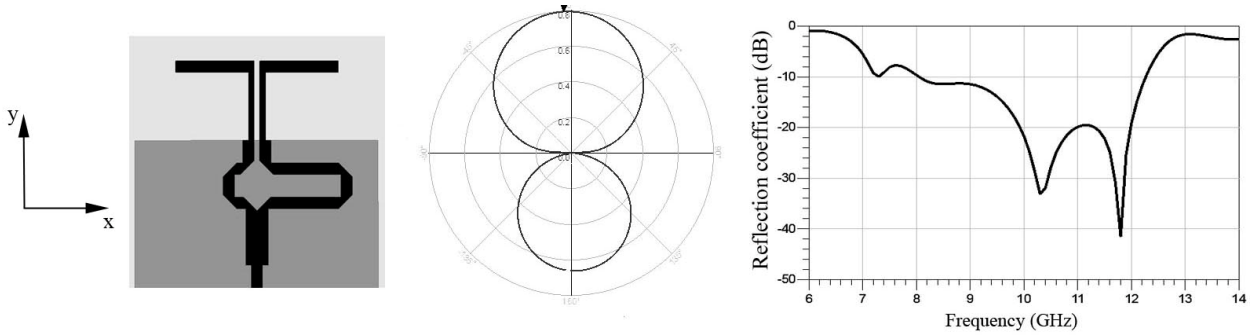

(a) ADS layout of dipole antenna (b) XZ cut at 9 GHz (c) Simulated input reflection coefficient

Fig. 37. ADS model of dipole antenna, XZ-cut and input reflection coefficient.

In this chapter a procedure to design antenna arrays using dipole elements is demonstrated. A broadside and tilted-beam were demonstrated in the XZ-plane radiation pattern. The next chapter describes the split ring antenna array design in the frequency range on 2-8 GHz.

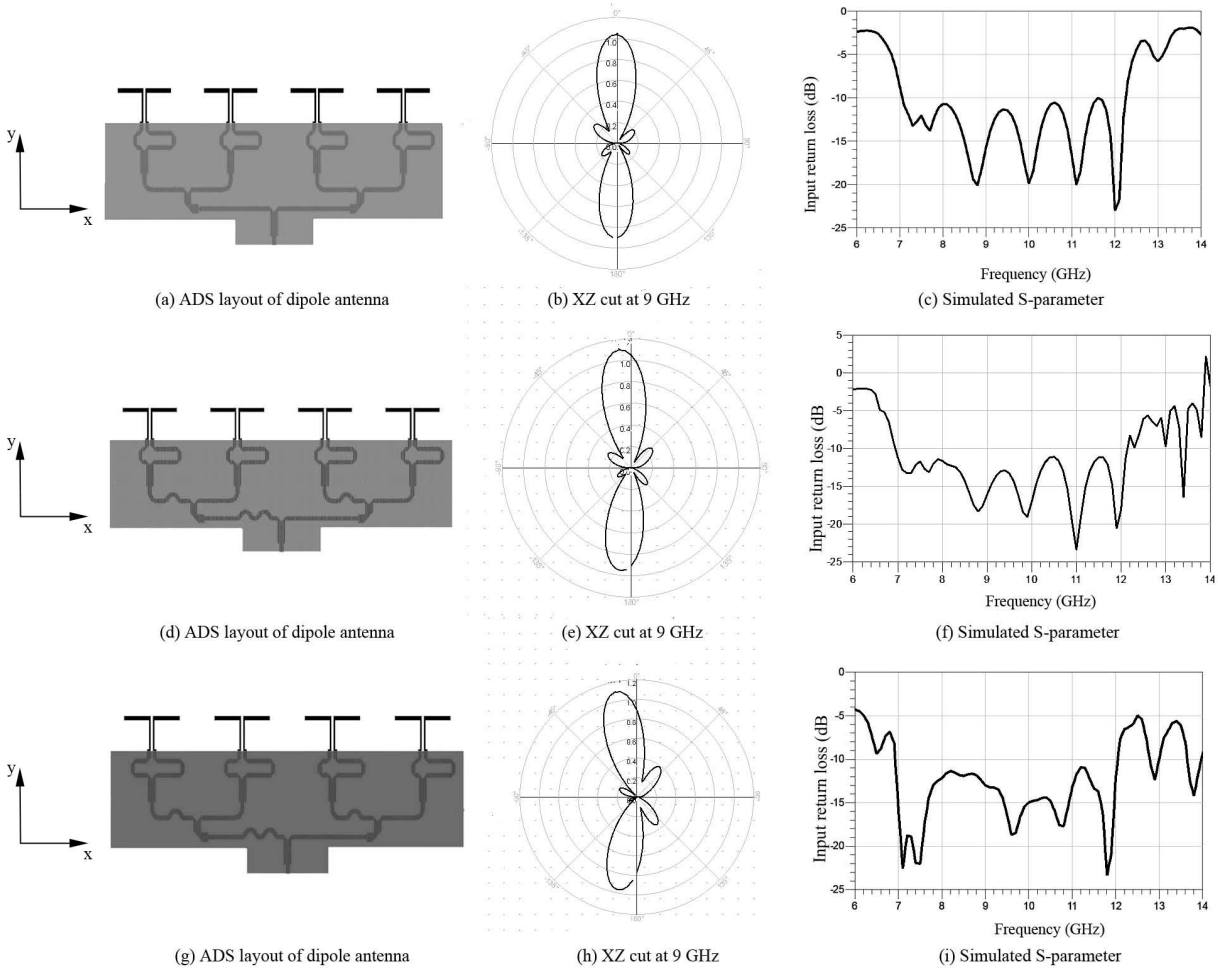

Fig. 38. Simulated input reflection coefficient and XZ-cuts of four element dipole antenna array: (a) Without beam steering (b) With meandering line beam steering (c) With meandering line beam steering plus additional beam steering from the phase shifter network.

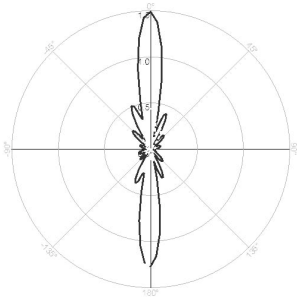

Fig. 39. Simulated XZ-cut of eight element dipole antenna array at 9 GHz.

CHAPTER 5. SPLIT-RING ANTENNA ARRAY

To meet an increasing data rate usage by devices such as by smartphones, tablets, and other mobile devices an antenna should have the ability to meet the needed coverage and capacity. Typically the power consumption and interference increases when omnidirectional antennas transmit signals in directions other than that of the desired user [33, 34]. By putting antenna elements in an array, a directive beam, with reduced interference in the network, can be achieved. In this section, we explore the split-ring antenna in an array environment. A simple four-element linear array is used to demonstrate the viability of the split-ring as an array antenna. Two proposed models of passive arrays are shown Fig. 40 and Fig. 41. The first is made of four identical antennas equally spaced along the axis perpendicular to the direction of maximum radiation, and all the elements are fed with equal magnitude of power with the same phase. This results in an array pattern known as a broadside array. The second uses microstrip delay lines to realize a progressive phase shift so that the main beam is tilted to a few degrees from broadside.

Each array is fabricated on a single piece of RT/Duroid substrate with effective dielectric of 10.2 and a material thickness of 1.27 mm. The horizontal center-to-center spacing is 35 mm. This corresponds to $0.6\lambda_g$ at the center frequency of the antenna. Photographs of the arrays are shown in Fig. 42 and Fig. 43. The width of each board is approximately 13.3 cm. The array utilizes a simple feed system composed of T-junctions and quarter-wave impedance transformers. The 50-Ω microstrip lines of the elements are joined at a T-junction and transformed through a 35-Ω quarter-wave transformer back to a single 50-Ω line at 5 GHz design frequency. The measured input reflection coefficients of the broadside and tilted version of the

antennas are shown in Fig. 44. The measured frequency bandwidth is approximately 110% for a VSWR ≤ 2.

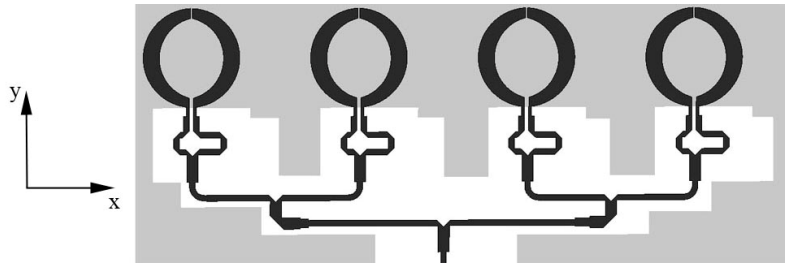

Fig. 40. ADS layout of four-element split-ring antenna array for broadside beam.

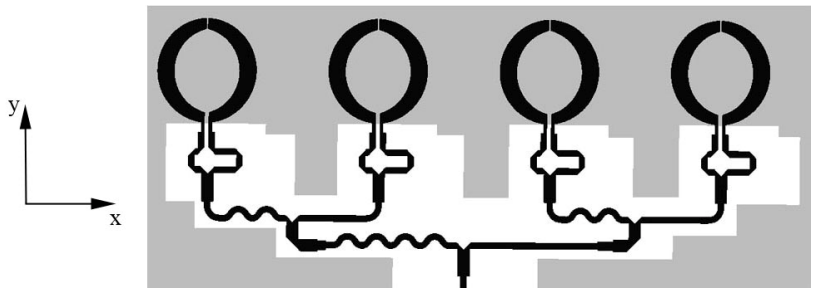

Fig. 41. ADS layout of four-element split-ring antenna array with delay lines for tilted beam.

The broadside and tilted radiation patterns have been measured at three different frequencies: 2.5, 4.5 and 6.5 GHz, corresponding to the lower end, center, and upper end frequencies of the operating band of the antenna as shown in Figs. 45 and 46 respectively. The measured XZ-cut and YZ-cut radiation patterns of the arrays are in close agreement with the simulated patterns.

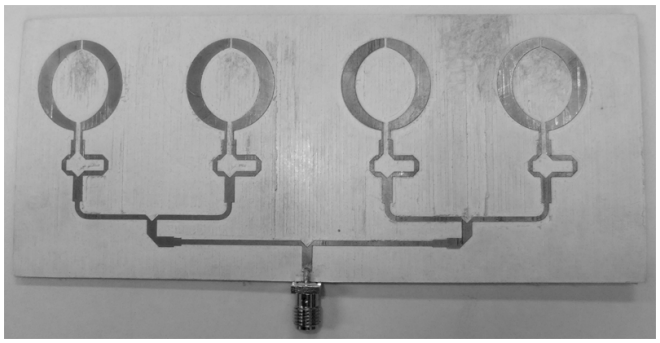

Fig. 42. Photograph of four-element split-ring antenna array for broadside beam.

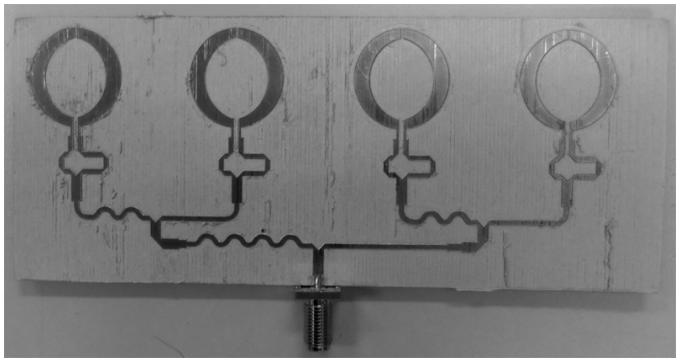

Fig. 43. Photograph of four-element split-ring antenna array with delay lines for broadside beam.

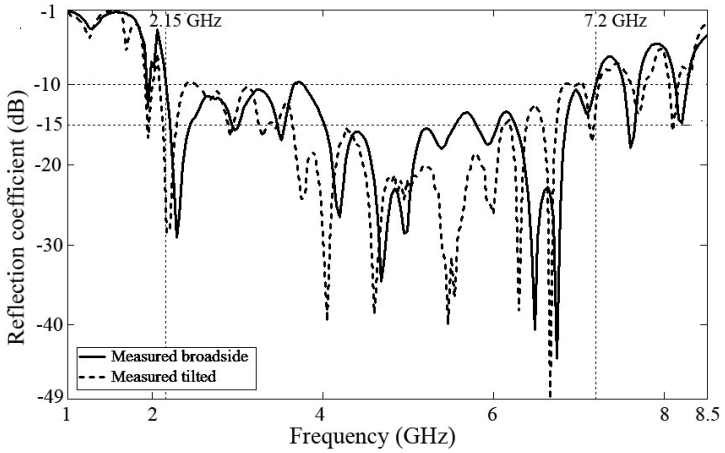

Fig. 44. Measured input reflection coefficient for broadside and tilted beam of split-ring antenna arrays.

The frequency range of 2 to 8 GHz corresponds to λ_g of 55-14 mm. The center-to-center element spacing is 35 mm (λ_{35}), which is one guided wavelength at approximately 3.2 GHz. Therefore side lobes can be expected above 3.2 GHz. Measured and simulated radiation patterns for the broadside and tilted arrays at 2.5 GHz and 4.5 GHz are shown in Fig. 47. Linear scale magnitude plots are presented because beams are broad in nature, and it is difficult to demonstrate beam steering with a dB scale. For these particular frequencies, the scan angle is 7.2 degrees at 2.5 GHz and 11 degrees at 4.5 GHz is achieved. Beam steering is not shown above 4.5 GHz because of the generation of excessive side lobes make it difficult to demonstrate beam

steering. Decreasing the element separation can avoid generating side lobes at higher frequencies; however the reason for choosing 35 mm element center-to-center spacing is to have enough space to implement horizontal meandering lines. This work is mainly to show that it is possible to design arrays using a split-ring antenna.

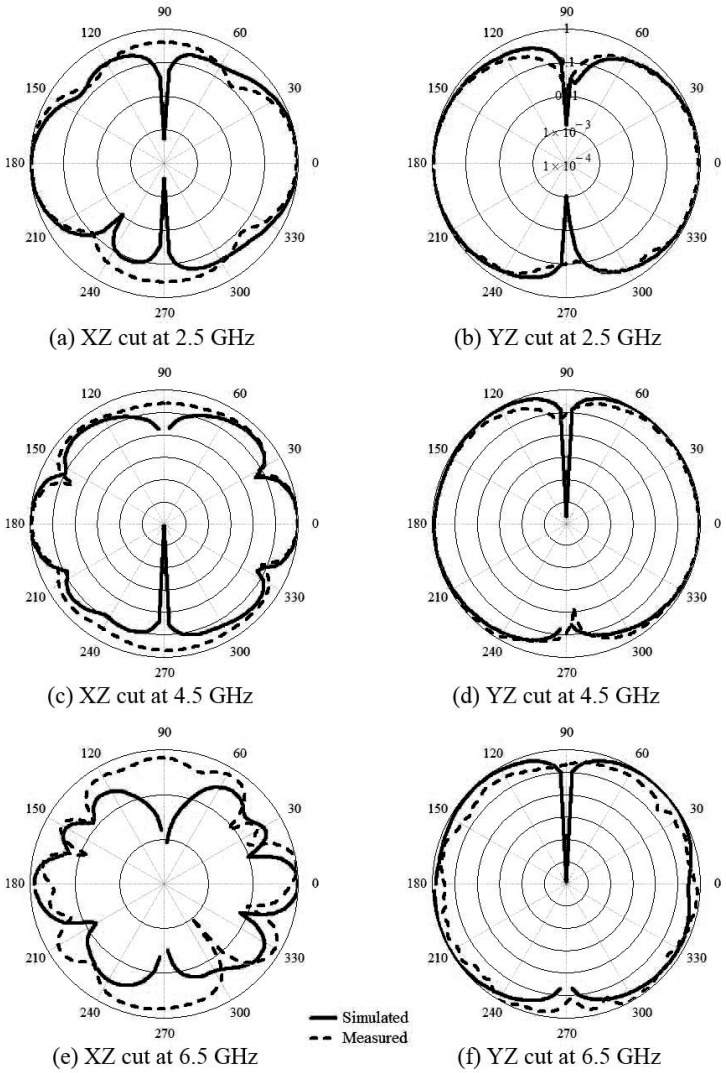

(a) XZ cut at 2.5 GHz (b) YZ cut at 2.5 GHz

(c) XZ cut at 4.5 GHz (d) YZ cut at 4.5 GHz

(e) XZ cut at 6.5 GHz (f) YZ cut at 6.5 GHz

Fig. 45. Measured and simulated radiation patterns of split-ring antenna broadside-beam array at 2.5, 4.5 and 6.5 GHz.

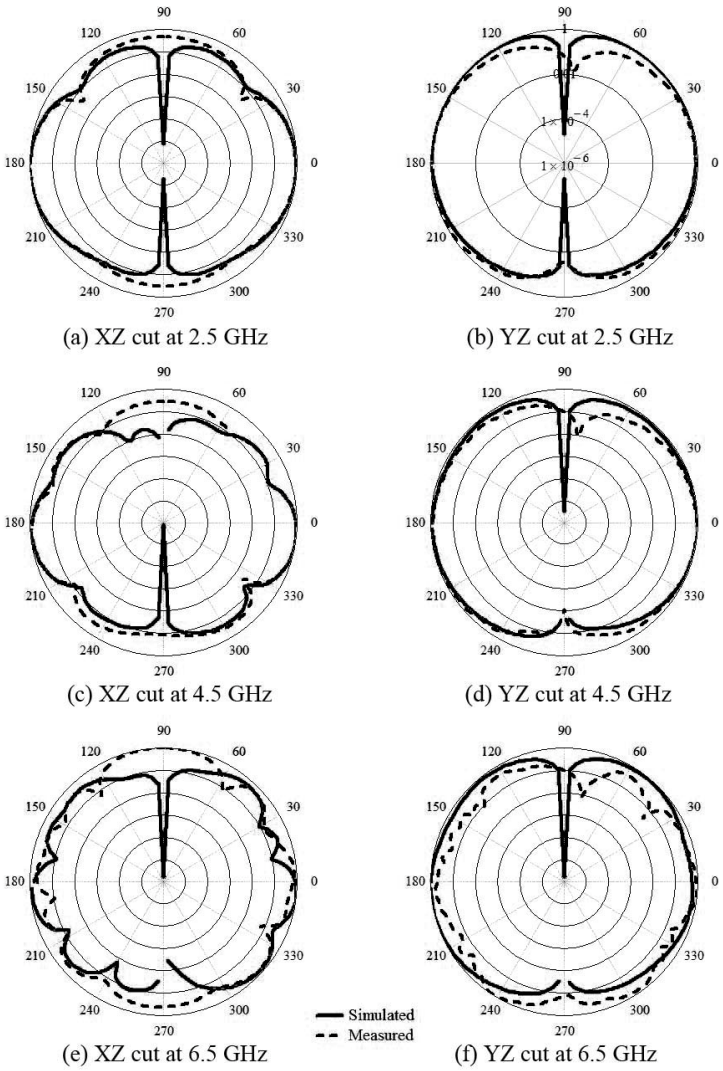

Fig. 46. Measured and simulated radiation patterns of split-ring antenna broadside-beam array at 2.5, 4.5, 6.5 and 7.5 GHz.

Finally, the simulated gain of one element and of the arrays has been compared from 2 to 8 GHz, and is shown in Fig. 48. The single element gain varies from - 3.6 dBi to 0.9 dBi, while the array gain varies from 3.5 to 7 dBi, for the entire passband. Moreover, the variation in gain between the broadside array and the tilted beam array is extremely small. This means that the overall antenna performance (reflected power, radiation pattern and gain) of the split-ring array

is good, and is not seriously affected by phenomena such scan blindness, mutual coupling and surface

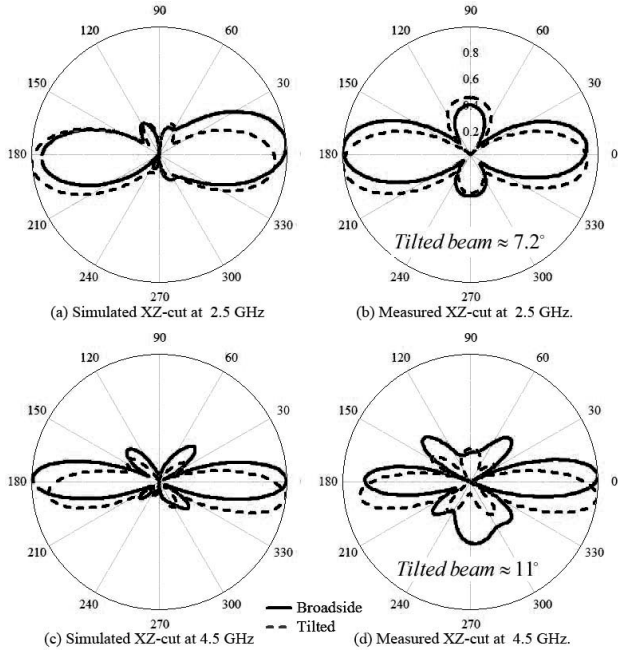

Fig. 47. Broadside and tilted-beams radiation patterns at 2.5 and 4.5 GHz.

waves [22, 23, 24]. Since the simulated and measured radiation patterns in both XZ- and YZ-planes are in good agreement across the entire frequency band, the simulated gain in general should have a good agreement with the actual gain. Nearly omnidirectional patterns have been observed in YZ-plane. In the XZ-plane the radiation pattern is more bi-directional with side lobes.

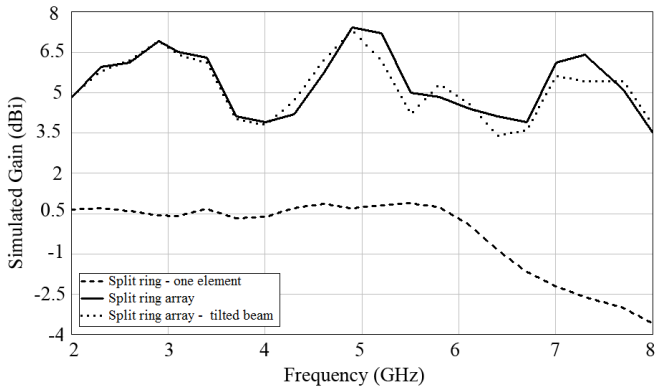

Fig. 48. Simulated relative gain along the z-axis.

A four-element linear split-ring antenna array may find applications in situations requiring long distance and wide area communication coverage. The antenna elements were slightly modified to take into account the mutual coupling among these elements. It was found that the mutual coupling has shrunk the bandwidth slightly. The next chapter briefly describes the fabrication and measurement of the antennas.

CHAPTER 6. FABRICATION AND MEASUREMENT

The prototype of the proposed antenna has been fabricated on a RT/duroid 6010LM substrate, Rogers Corporation's high frequency circuit material with a dielectric constant of 10.2 and a loss tangent of 0.0023, with a dielectric thickness of 1.27 mm. The radiation patterns are obtained by an automatic measurement system in an anechoic chamber as shown in Fig. 49 . Various antennas mounted on a swivel are shown in Fig. 50, Fig. 51 and Fig. 52. The basic procedure is to rotate the receiver antenna in the field of the transmitter antenna and record the results over the entire 360° range. Often this procedure is performed in an anechoic chamber to eliminate environmental noise or reflections that would alter the receiving antenna's response. The radiation patterns observed in XZ-and YZ-planes in ADS are illustrated in Fig. 53. Fig. 54. shows the ADS split-ring antenna array model with the 3D radiation pattern.

Fig. 49. Anechoic chamber used for antenna measurement.

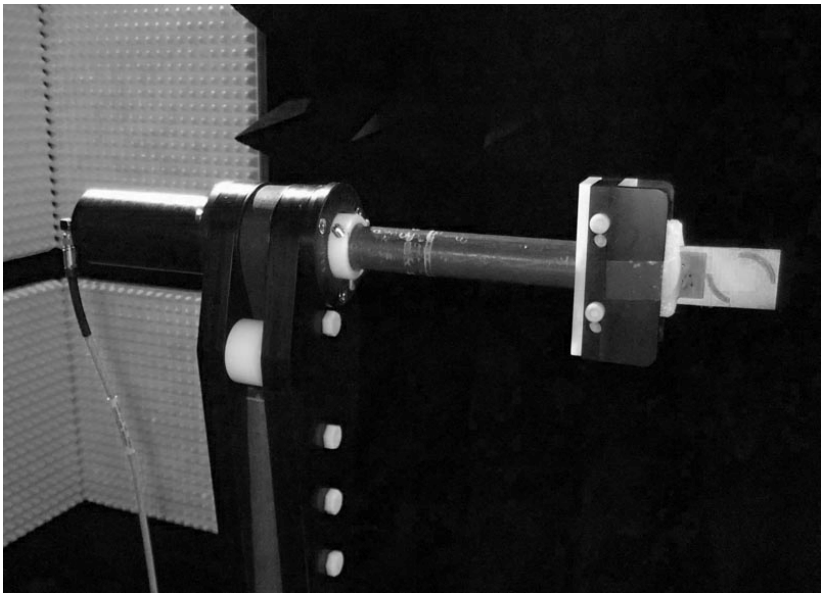

Fig. 50. Segmented-ring antenna mounting system.

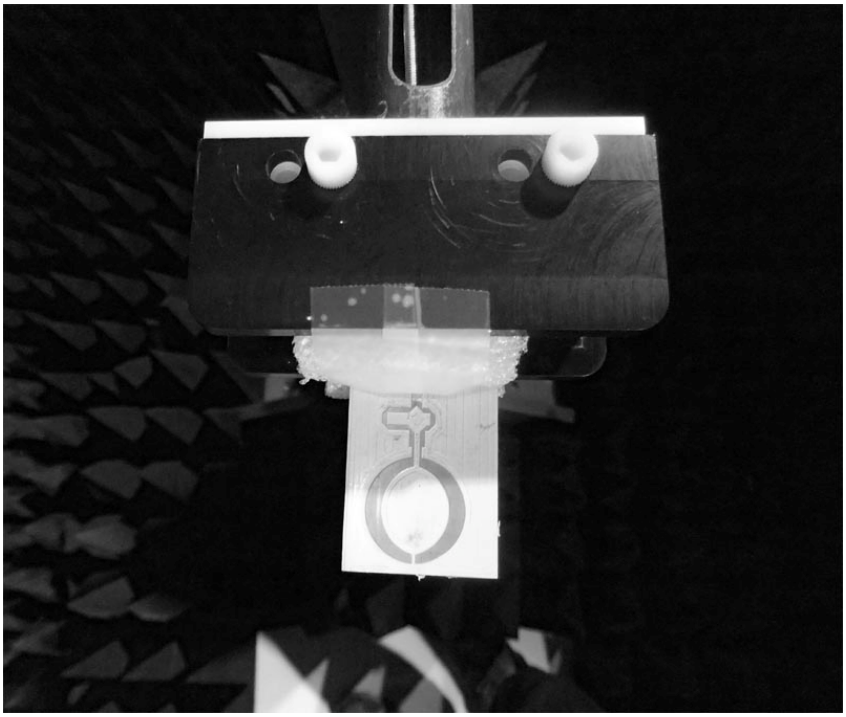

Fig. 51. Close-up view of split-ring antenna mounting system.

Fig. 52. Close-up view of split-ring antenna array mounting system.

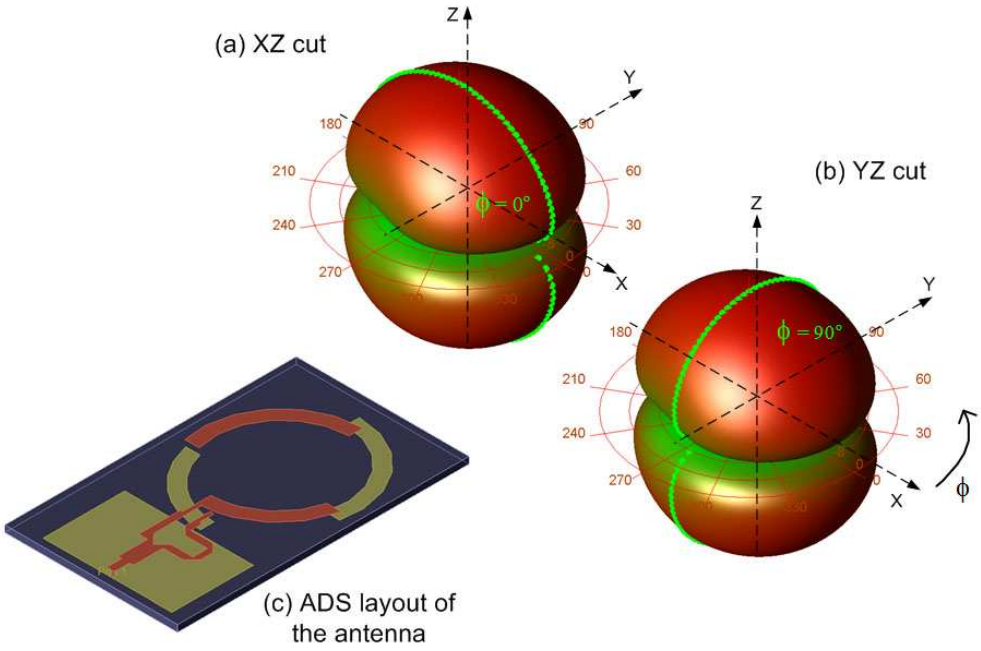

Fig. 53. ADS model segmented ring antenna, XZ-cut and YZ-cut.

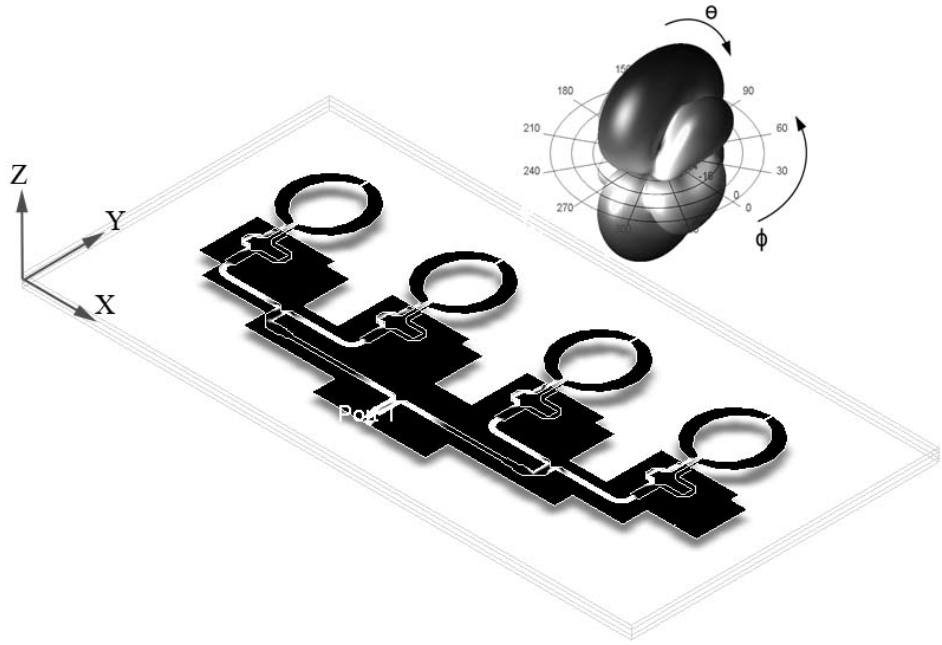

Fig. 54. ADS split-ring antenna array model.

CHAPTER 7. DISCUSSION AND CONCLUSION

A new segmented ring antenna and a split-ring array have been presented, as well as two arrays using the split-ring antenna as a radiating element. Both antennas achieve an extremely wide frequency bandwidth and good radiation characteristics in terms of beam pattern. The variation in gains of the split-ring antenna is smaller and is more stable compared with the segmented-ring antenna. Moreover, the size of the split-ring antenna is smaller and has a broader radiation pattern than the segmented ring antenna. In the wideband system it is very hard to achieve a perfect match over a wide frequency match so a VSWR ≤ 2 is considered good matching.

The split ring antenna element gain varies from - 3.6 dBi to 0.9 dBi, while the array gain varies from 3.5 to 7 dBi for the entire passband. On average, the array has improved the directive gain by approximately 7 dBi. This means that the overall radiation efficiency of the array is good, and is not seriously affected by phenomena such as scan blindness, mutual couplings and surface waves [27, 28, 29]. The antenna element experimentally demonstrated a bandwidth of 120% while the arrays achieved 110% for the VSWR ≤ 2.

The excellent radiation properties and compact size of this antenna make it ideal as either a standalone antenna with a broad radiation pattern or as an array element. We have presented two simple arrays using the split-ring antenna. Both of the two four-element arrays are fabricated on a single substrate, which can be used as a building block for a larger planar or 2-D array or as a standalone base station antenna with a broadside beam radiation pattern. Future work includes shrinking the size of the array by reducing the center-to-center spacing so that side lobes can be kept as low at the higher frequency end of the passband. Segmented rings are

another promising way for enhancing bandwidth, and implementing antenna arrays of various kind. The broadside array is bidirectional in symmetrical pattern and can be used for long distance communication where directivity needs to be strong.

The split-ring antenna has several advantages over the segmented-ring antenna. First, the realized split-ring antenna eliminated all the via-less capacitive couplings. Secondly, a broader radiation pattern with more stable gain is achieved. The net result is all radiator elements are moved to the top side of the substrate. The antenna is implemented on the same dielectric substrate material and thickness with a microstrip feed occupying a smaller area compared with segmented ring antenna.

BIBLIOGRAPHY

[1] M. Rafee Aghda, M. F. B. Ain, and A. B. Md. Shahar," A New Ultra-wideband Antenna With Unique Ground Plane Shape", *Progress In Electromagnetics Research Letters*, Vol. 35, 165-179, 2012.

[2] Minh-Chau Huynh, *Wideband Compact Antennas for Wireless Communication Applications*, Thesis (PhD), Virginia Polytechnic Institute and State University, Nov. 22, 2004.

[3] Peter Knott, *Design of a Printed Dipole Antenna Array for a Passive Radar System*, Dept. of Antenna Technology and Electromagnetic Modelling (AEM), Fraunhofer Institute for High Frequency, RWTH Aachen University, 19 April 2013

[4] Jing Jin,"Ultra-Wideband (UWB)", Communications Engineering Laboratory, HUT. www.cse.tkk.fi/fi/opinnot/T-109.7510/2006/UWB.doc

[5] Directional propagation channels, www.madhur.co.in/files/Ultrawideband.ppt.

[6] Gabriela quintero díaz de león, "Analysis and Design of Ultra-Wideband Antennas in the Spectral and Temporal Domains", Thesis, école polytechnique fédérale de lausanne, 2010.

[7] "Spectrum Allocations for Ultra Wide Band Communication Devices", A Discussion Paper, April 2008.

[8] "International Spectrum Allocation for UWB Bands", 2009.

[9] en.wikipedia.org/wiki/File:International_Spectrum_Allocation_for_UWB_Bands_2009.gif.

[10] R.L. Yadava, *Antenna & Wave Propagation*, Phi Learning Pvt. Ltd. Nov 1, 2011.

[11] Zhi-Ya Zhang,Cheng-Bin Zhang, "Wideband omnidirectional printed dipole antenna with coupling feed for wireless communication applications", *Progress In Electromagnetics Research C*, Vol. 38, 89 - 99, 2013.

[12] Giovanni A. Casula, Paolo Maxia, Giuseppe Mazzarella, and Giorgio Montisci, "Design of a printed log-periodic dipole array for ultra-wideband applications" *Progress In Electromagnetics Research C*, Vol. 38, 15-26, 2013.

[13] Rmili H., Floc'h J. M., "Design and analysis of wideband double-sided printed spiral dipole antenna with capacitive coupling", *Microwave and Optical Technology Letters*, vol 50, No.5, 1312-1317, 2008.

[14] Tourette, S., Fortino, N., Kossiavas, G.,"Compact UWB printed antennas for low frequency applications matched to different transmission lines", *Microwave and Optical Technology Letters*, Vol. 49, No.6,1282-1287.2006.

[15] Zhang, X., Wu, W., Yan, Z. H., Jiang, J. B. & Song, Y,"Design of CPW-Fed monopole UWB antenna with a novel notched ground", *Microwave and Optical Technology Letters*,Vol. 51, No.1, 88-91,2009.

[16] Abhishek Agrawal, Himanshu Joshi," Rectangular Microstrip Patch Antenna for S-Band and C- Band Application*", International Journal of Review in Electronics & Communication Engineering (IJRECE)*, Volume 1 - Issue 2, June 2013.

[17] Hossein Malekpoor and Shahrokh Jam, "Enhanced Bandwidth of Shorted Patch Antennas Using Folded-Patch Techniques" *IEEE Antennas and Wireless Propagation Letters*, Volume 12, 2013.

[18] F. D. Dahalan, S. K. A. Rahim, M. R. Hamid, M. A. Rahman, M. Z. M. Nor, M. S. A. Rani, and P. S. Hall, "Frequency-Reconfigurable Archimedean Spiral Antenna ", *IEEE Antennas and Wireless Propagation Letters*, Vol. 12, 2013.

[19] J.A.Ansari, Kamakshi, Ashish Singh, Anura Mishra,"Analysis of Ultra-Wideband Patch Antenna for S, C & X Band Applications", *International Conference on Computer & Communication Technology (ICCCT)*, 2011.

[20] William R. Deal, Noriaki Kaneda, James Sor, Yongxi Qian, and Tatsuo Itoh, "A New Quasi-Yagi Antenna for Planar Active Antenna Arrays", *IEEE Transactions on Microwave Theory and Techniques*, Vol. 48, No. 6, June 2000.

[21] Thorsten W. Hertel, and Glenn S. Smith, "Analysis and Design of Two-Arm Conical Spiral Antennas", *IEEE Transactions on Electromagnetic Compatibilty*,Vol. 48, No. 6, June 2000.

[22] Michel Clénet ”Design and analysis of a Yagi-like antenna element buried in LTCC material for AEHF communication systems”, Technical Memorandum, DRDC Ottawa TM 2005-055, April 2005.

[23] Bruce Carter, Ron Mancini, Op Amps for Everyone, Chapter 17, Circuit Board Layout Techniques, Third Edition, March 4, 2009.

[24] Warren L. Stutzman, Gary A. Thiele, *Antenna Theory and Design*, second edition, JohnWiley & Sons, Inc., 1998.

[25] David M. Pozar, *Microwave Engineering*, 3rd Edition,John Wiley & Sons, Inc., 2000-2013.

[26] Ben Allen, Mischa Dohler, Ernest E. Okon, Wasim Q. Malik, Anthony K. Brown and David J. Edwards, *Ultra-wideband Antennas and Propagation for Communications, Radar and Imaging*, John Wiley & Sons, 2007.

[27] A. Sharma and G. Singh,”Design of single pin shorted three-dielectric-layered substrates rectangular patch microstrip antenna for communication systems”, *Progress In Electromagnetics Research Letters*, Vol. 2, 157–165, 2008.

[28] J.R. James and P.S. Hall,”Handbook of Microstrip Antennas (IEE Electromagnetic Waves Series”, *The Institution of Engineering and Technology*; 2-Vol edition (December 1989).

[29] C. A. Balanis, *Antenna Theory*, third edition, Wiley, 2005.

[30] Fredrik Gulbrandsen, *Design and Analysis of an X-band Phased Array Patch Antenna", Norwegian University of Science and Technology,* Thesis, 2013.

[31] Natalia K. Nikolova, "Modern Antennas in Wireless Telecommunications", Department of Electrical and Computer Engineering, McMaster University, www.ece.mcmaster.ca/faculty/nikolova.

[32] R. JaNNaH, "Printed dipole antenna", www.scribd.com/doc/20912139/Printed-Dipole-Antenna.

[33] Basic yagi antenna design for the experimenter, www.hamuniverse.com/yagibasics.html.

[34] Frank Gross, *Smart Antenna for Wireless Communication*, McGraw-Hill, (2005).

[35] Angeliki Alexiou and Martin Haardt, "Smart Antenna Technologies for Future Wireless Systems: Trends and Challenges", *IEEE Communication Magazine*, Vol. 42, No.9, 90-97, 2004.

[36] Fawwaz T. Ulaby, *Fundamentals of Applied Electromagnetics*, 5th edition, January 1, 2006.

APPENDIX A. DERIVATION OF THE FAR-FIELD ELECTRIC FIELD.

Short Dipole

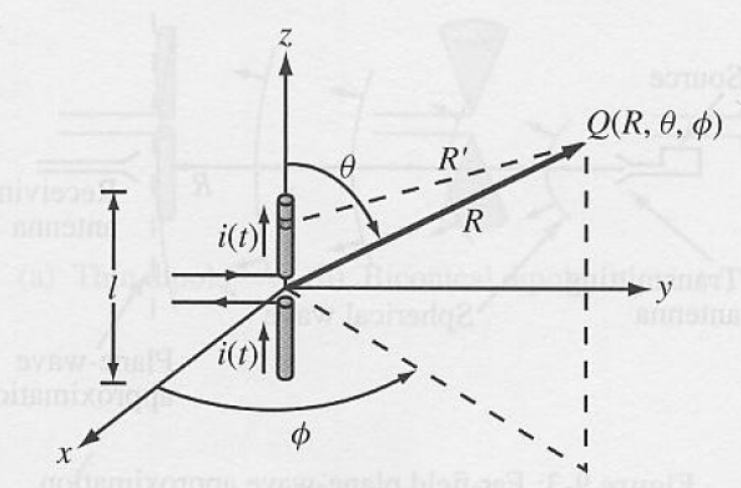

Fig. A1. Short dipole placed at the origin of a spherical coordinate system. Adapted from *Fundamentals of Applied Electromagnetics* (page 376), by Fawwaz T. Ulaby, 2006, Upper Saddle River, N.J: Pearson Prentice Hall.

A short dipole (a differential antenna), also called a Hertzian dipole, is a thin linear conductor whole length where ***l*** is very short compared with the wavelength λ. The far-far field expression for a short dipole is given in (A.1) [35]. The function e^{-jkR}/R is the spherical propagation factor and accounts for the 1/R decay of the magnitude with distance as well as for the phase change represented by e^{-jkR}.

$$\tilde{E}_\theta = \frac{jI_0 lk\eta_0}{4\pi}\left[\frac{e^{-jkR}}{R}\right] sin\theta \quad (\mathrm{V/m}) \tag{A.1}$$

Dipole of Arbitrary Length

For a center-fed dipole, as depicted in Fig. A2 [35], the currents flowing through its two halves are symmetrical and must go to zero at its ends. Therefore the current phasor $\tilde{I}(z)$ can be expressed as a piecewise continuous sine function where I_0 is the current amplitude as shown in (A.2).

$$\tilde{I}(z)=\begin{Bmatrix} I_0 \sin\left[k\left(\frac{l}{2}-z\right)\right], & for\ 0\le z\le \frac{l}{2} \\ I_0 \sin\left[k\left(\frac{l}{2}+z\right)\right], & for -\frac{l}{2}\le z\le 0 \end{Bmatrix}. \tag{A.2}$$

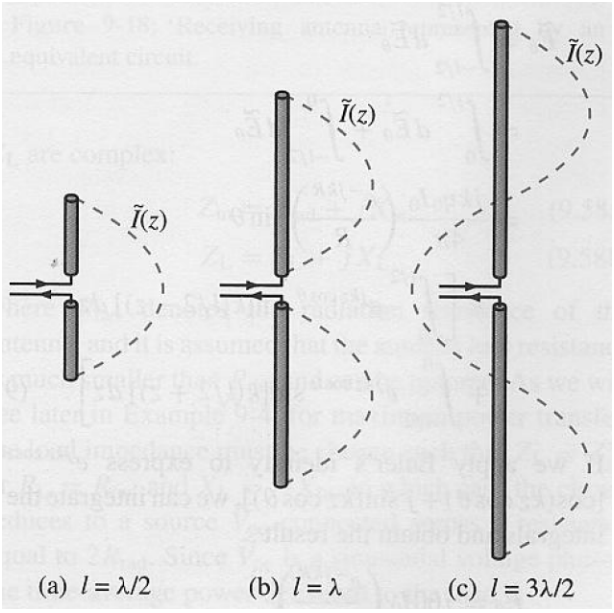

Fig. A2. Current distribution for three center-fed dipoles. Adapted from *Fundamentals of Applied Electromagnetics* (page 391), by Fawwaz T. Ulaby, 2006, Upper Saddle River, N.J., Pearson Prentice Hall.

The Hertzian dipole expression can be used as a building block to obtain expressions for the field radiated by dipole antenna of arbitrary length *(l).* Fig. A3 shows a center-fed thin wire

dipole of length *l*. Using the expression (Hertzian E-field) for an infinitesimal dipole segment of length *dz*, excited by a current $\tilde{I}(z)$ and located at a distance *s* from the observation point (Fig. A3b), the differential E-field can be expressed as

$$d\tilde{E}_\theta = \frac{jk\eta_0}{4\pi}\tilde{I}(z)dz\left[\frac{e^{-jks}}{s}\right]\sin\theta_s \tag{A.3}$$

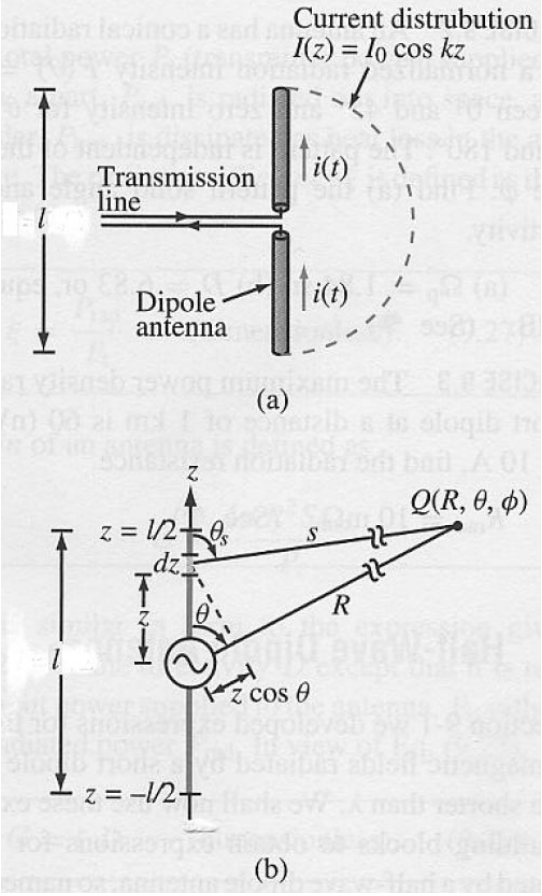

Fig. A3. Center-fed dipole of length *l*. Adapted from *Fundamentals of Applied Electromagnetics* (page 388), by Fawwaz T. Ulaby, 2006, Upper Saddle River, N.J: Pearson Prentice Hall.

The far field due to radiation by the entire antenna is obtained by integrating the fields from the Hertzian dipoles making up the antenna:

$$\tilde{E}_\theta = \int_{l/2}^{l/2} d\tilde{E}_\theta . \tag{A.4}$$

Two approximations are necessary before evaluating (A.4). Firstly, the distance *s* is considered to be much larger than the length of the dipole so that the difference between *s* and *R* may neglected in terms of its effect on *1/s*. Thus $1/s \approx 1/R$ and $\theta_s \approx \theta$. For the phase factor e^{-jks}, approximating s ≈ R can introduce significant phase error [34]. An acceptable approximation is

$$s = R - z\cos\theta \tag{A.5}$$

Substituting (A.5) for s in the phase factor of (A.3) and *s* with *R* and θ_s with θ gives [34]

$$d\tilde{E}_\theta = \frac{jk\eta_0}{4\pi}\tilde{I}(z)dz\left[\frac{e^{-jkR}}{R}\right]\sin\theta\, e^{jkz\cos\theta} \tag{A.6}$$

Inserting expression $\tilde{I}(z)$ given by (A.2) in (A.6) results in

$$d\tilde{E}_\theta = \frac{jk\eta_0}{4\pi}\left[\frac{e^{-jkR}}{R}\right]\sin\theta\, e^{jkz\cos\theta}\,\tilde{I}(z)\,dz$$

where

$$\tilde{I}(z) = \begin{Bmatrix} I_0 \sin\left[k\left(\frac{l}{2} - z\right)\right], & for\ \ 0 \le z \le \frac{l}{2} \\ I_0 \sin\left[k\left(\frac{l}{2} + z\right)\right], & for -\frac{l}{2} \le z \le 0 \end{Bmatrix}. \tag{A.7}$$

The total field radiated by the dipole is

$$\tilde{E}_\theta = \int_{l/2}^{l/2} d\tilde{E}_\theta$$
$$= \int_{0}^{l/2} d\tilde{E}_\theta + \int_{-l/2}^{0} d\tilde{E}_\theta$$
$$= \frac{jk\eta_0 I_0}{4\pi}\left(\frac{e^{-jkR}}{R}\right)\sin\theta \times \left[\int_0^{l/2} e^{jkz\cos\theta}\sin\left[k\left(\frac{l}{2}-z\right)\right] + \int_{-l/2}^{0} e^{jkz\cos\theta}\sin\left[k\left(\frac{l}{2}+z\right)\right]\right] \quad \text{(A.8)}$$

Using the identity

$$\int \sin(a+bz)e^{cz}dx = \frac{e^{cz}}{b^2+c^2}\left[c\sin(a+bz) - b\cos(a+bz)\right]$$

with $a = k\,l/2 \;\; b = \pm k \;\; c = jk\cos\theta,$ (A.9)

the integral in (A.8) can be expressed as follows

$$\tilde{E}_\theta = \frac{jk\eta_0 I_0}{4\pi}\left(\frac{e^{-jkR}}{R}\right)\sin\theta$$
$$\times\left(\frac{1}{k^2 - k^2\cos^2\theta}\right)\left[\begin{array}{l}\left\{e^{jkz\cos\theta}\left[jk\cos\theta\sin k(l/2 - z) + k\cos k(l/2 - z)\right]\right\}_0^{l/2} + \\ \left\{e^{jkz\cos\theta}\left[jk\cos\theta\sin k(l/2 + z) - k\cos k(l/2 + z)\right]\right\}_{-l/2}^{0}\end{array}\right]. \quad \text{(A.10)}$$

Evaluating the upper and lower limits over the entire length gives (A.11)

$$\tilde{E}_\theta = \frac{jk\eta_0 I_0}{4\pi}\left(\frac{e^{-jkR}}{R}\right)\sin\theta \times \left(\frac{1}{k^2 - k^2\cos^2\theta}\right)\left[\begin{array}{l}ke^{\frac{jkl}{2}\cos\theta} - jk\cos\theta\sin k(l/2\;) - k\cos k(l/2) + \\ \left\{\left(jk\cos\theta\sin k(l/2) - k\cos k(l/2)\right) + ke^{-\frac{jkl}{2}\cos\theta}\right\}\end{array}\right]$$
$$= \frac{jk\eta_0 I_0}{4\pi}\left(\frac{e^{-jkR}}{R}\right)\sin\theta \times \left(\frac{1}{k^2\sin^2\theta}\right)\left[ke^{\frac{jkl}{2}\cos\theta} + ke^{-\frac{jkl}{2}\cos\theta} - 2k\cos k(l/2\right]$$
$$= \frac{j\eta_0 I_0}{4\pi}\left(\frac{e^{-jkR}}{R}\right)\left(\frac{1}{\sin\theta}\right)\left[e^{\frac{jkl}{2}\cos\theta} + e^{-\frac{jkl}{2}\cos\theta} - 2\cos k(l/2\right] \quad \text{(A.11)}$$

Using the Euler's identity, (A.11) further simplifies to

$$\tilde{E}_\theta = \frac{j\eta_0 I_0 e^{-jkR}}{4\pi R}\frac{\left[2\cos\left(\frac{kl}{2}\cos\theta\right) - 2\cos k(l/2)\right]}{\sin\theta}$$

$$= \frac{j\eta_0 I_0 e^{-jkR}}{2\pi R}\frac{\left[\cos\left(\frac{kl}{2}\cos\theta\right) - \cos k(l/2)\right]}{\sin\theta} \qquad \text{(A.12)}$$

APPENDIX B. DERIVATION OF SEGMENTED-RING ANTENNA CIRCUIT MODEL SHOWN IN FIG. 19.

The input impedance (Z_{in}) looking into terminal 1-2 in Fig. 19 is:

$$
\begin{aligned}
Z_{in} &= \frac{j\omega L_1}{2} + \frac{R_1}{2} + \left\{ \left(\frac{1}{j\omega C_{sh}} \right) // \left(\frac{1}{j\omega C_{c1}} + R_1 + j\omega L_2 \right) \right\} + \frac{j\omega L_1}{2} + \frac{R_1}{2} \\
&= j\omega L_1 + R_1 + \left\{ \left(\frac{1}{j\omega C_{sh}} \right) // \left(\frac{1}{j\omega C_{c1}} + R_1 + j\omega L_2 \right) \right\} \\
&= j\omega L_1 + R_1 + \left\{ \left(\frac{1}{j\omega C_{sh}} \right) // \left(\frac{1}{j\omega C_{c1}} + R_1 + j\omega L_2 \right) \right\} \\
&= j\omega L_1 + R_1 + \frac{\left(\frac{1}{j\omega C_{sh}} \right) \left(\frac{1}{j\omega C_{c1}} + R_1 + j\omega L_2 \right)}{\left(\frac{1}{j\omega C_{sh}} + \frac{1}{j\omega C_{c1}} + R_1 + j\omega L_2 \right)}.
\end{aligned}
\tag{B.1}
$$

Thus,

$$
Z_{in} = j\omega L_1 + R_1 + \frac{R_2 + j\left[\omega L_2 - \frac{1}{\omega C_{c1}} \right]}{1 + \frac{C_{sh}}{C_{c1}} - \omega^2 L_2 C_{sh} + j\omega C_{sh} R_2} \tag{B.2}
$$